LÉVY NOISE INDUCED STEADY STATES.

By

Steven Yuvan

July, 2022

Dissertation Director: Martin Bier

Department of Physics

ABSTRACT

Systems far from equilibrium organize themselves to accommodate energy throughput. It is also in these nonequilibrium systems where noise has often been found to follow alpha-stable distributions, commonly called Lévy noise, rather than Gaussian distributions. There is no general theory that links these alpha-stable distributions to the resultant thermodynamic behavior of a system as a whole. Here two different model systems are investigated for which the assumption of Lévy noise leads to behavior that deviates from that seen at equilibrium. We begin by examining trajectories of overdamped noise-driven particles in a harmonic potential. These trajectories display broken time reversal symmetry due to the large displacements inherent to Lévy noise. A parameter to measure this symmetry breaking and estimate the stability parameter, α, of the underlying noise is proposed. This parameter is applied to a time series of solar x-ray irradiance and compared to previous methods.

Next, we study the same overdamped particles in a 2D system with simple semi-circular cavities. Lévy noise in such a system will lead to a preferential accumulation of particles in one cavity. The nonhomogeneous steady-state represents a lower entropy configuration in comparison to equilibrium. The chosen system leads to concise expressions for the distribution of particles within the cavities as well as the concomitant entropy reduction. Such structures maintained in nonequilibrium have been referred to as dissipative structures because they may aid the system in transporting or dissipating energy.

Lévy noise induced steady states

A Disseration

Presented To the Faculty of the Department of Physics

East Carolina University

In Partial Fulfillment of the Requirements for the Degree

Ph.D. in Biomedical Physics

by

Steven Yuvan

July, 2022

Lévy noise induced steady states

By

Steven Yuvan

APPROVED BY:

Director of Dissertation

_____
Martin Bier, Ph.D.

Committee Member

_____
Robert Corns, Ph.D.

Committee Member

_____
Regina DeWitt, Ph.D.

Committee Member

_____
Guglielmo Fucci, Ph.D.

Committee Member

_____
Łukasz Kuśmierz, Ph.D.

Committee Member

_____
Zi-Wei Lin, Ph.D.

Chair of the Department of Physics

_____
Jefferson Shinpaugh, Ph.D.

Dean of the Graduate School

_____
Paul J. Gemperline, Ph.D.

Contents

List of Figures

Chapter 1

Introduction

Physicists are busy exploring new frontiers in nonequilibrium physics thanks to increasingly affordable and available computing power. It is now possible to simultaneously simulate thousands of individual atoms on a single computer, tens to hundreds of thousands on dedicated servers [12], and tens of millions via super computers [13]. This has allowed probing of the microscopic dynamics of systems without the need to rely on traditional statistical assumptions of 'local' equilibrium. The spread of these often highly specialized experiments has not slowed the search for a more general understanding of nonequilibrium. There is almost too diverse an assortment of phenomena attributed to, or associated with, nonequilibrium. Some of the more prominent: turbulence, self-organized criticality, anomalous diffusion, 1/f noise, Lévy flights, and long range coherence. Despite such variety, there are still a few unifying characteristics to investigate.

First, what qualifies a system as 'equilibrium'? The strictest definition is that of 'global' equilibrium. A system in global equilibrium has no internal flows or progression of chemical or physical processes. For this equilibrium, there are no external inputs and there is no evolution in time. A literal reading may even try to exclude observation. In technical language, entropy is maximized. The entropy of a system, $S = k_b \ln \Omega$, is a statistical statement about its configuration. Ω represents the number of alternative configurations

that yield a system with the same macroscopic properties. If a system at every moment 'chooses' a nearby (similar) state at random, it will obviously tend towards macroscopic states for which the number of choices, Ω, is more numerous. When this can no longer occur because the maximum Ω has been reached, the system is said to be at equilibrium. For some processes such as thermalization (e.g. achieving a Maxwell-Boltzmann distribution of particle speeds) this can occur in nanoseconds, while others, say waiting for a pendulum to stop or a black hole to evaporate, may take (much) longer.

Entropy is an extensive variable, i.e. $S = S(E, V, N)$. Therefore, it can also increase by adding to the system – increasing its total energy, E, its size, S, or the number of particles, N. To truly be at equilibrium, a system must be completely and wholly isolated. Even if such a purely isolated system did exist, observing it would be a logical impossibility. Yet equilibrium assumptions are pervasive and overwhelmingly successful. Everything is technically nonequilibrium, but far fewer systems are far enough outside equilibrium to matter. Richard Feynman gave a more palatable explanation [14], equilibrium is when "all the fast things have happened but the slow things have not." The key consideration is that there are no processes playing out with a *timescale comparable to that of the laboratory.*

An incomplete but helpful rule is that a requirement for nonequilibrium phenomena is a significant production of entropy. This will often accompany the transport or transformation of energy through a system, for instance the current through a wire or the conversion of ATP to mechanical energy, as well as the mere re-organization of a system itself. That precisely these forces underlie the structures or patterns in the natural world was an idea conceived by Prigogine in the mid 1900s [15]. Intrigued by the ability of biological systems to maintain order in spite of brute thermodynamics, Prigogine showed that the inherent disordered stability (due to entropic forces) of systems near equilibrium can be turned on its head far from equilibrium. Counterintuitively, these systems seem to spontaneously generate and maintain ordered structures. Rivers can create whorls and air masses create convection currents. At its most eccentric, it has been suggested that life itself can be reduced to a very

complex dissipative structure. A more reserved reading suggests that our understanding of far-from-equilibrium-physics will need development if we are to ever describe such systems more than phenomenologically.

The reason for the stark divergence from the predictability of equilibrium systems, as Prigogine notes [15], is easy to understand. At equilibrium there are no flows or gradients ($\nabla \phi$). Thus to first order approximation, the familiar laws of statistical thermodynamics, say $J = -D\nabla\rho$ for diffusion, are linear so long as you are *near equilibrium*, i.e. near $J = 0$. They take the form of functions that are stable around the point of maximum entropy. Once these linear approximations begin to fail, this stability is threatened as well - as is the meaningfulness of entropy itself.

When exactly those failed approximations happen is not well understood - nor are the consequences. This work attempts to investigate this question by examining some simple systems on the microscopic level. We will operate by *assuming* nonequilibrium, through the adoption of certain noise distributions, and then analyze the consequences. The difference between equilibrium and nonequilibrium will first be discussed, with particular attention paid to these distributions. The common tools, the Langevin and Fokker-Planck equations, will then be introduced along with their nonequilibrium counterparts. Some background on classic noise processes and traditional methods for their analysis is also given. Finally, these tools are applied analytically and by simulation to two model systems - an overdamped particle in a potential and overdamped particles in a (semi)circular bath.

Chapter 2

Nonequilibrium on the Microscopic Scale

2.1 Time Reversal Symmetry and the Central Limit Theorem

The introduction alluded to the idea that although no system is truly in equilibrium (as there will always be *some* sort of process playing out) it is often good enough to assume equilibrium if all of the 'quick' processes have finished. One need not wait for the dust to settle to know a bomb has gone off. The ease at which systems achieve so-called 'local' equilibrium is closely related to the speed of convergence of the central limit theorem (CLT). This theorem roughly states that the additive result of many random inputs will be a Gaussian in distribution: near equilibrium, noise is Gaussian. It can be most easily demonstrated through use of characteristic functions. For a distribution $X(t)$, its characteristic function is defined as:

$$\tilde{X}(k) = \mathbb{E}[e^{ikX}] = \int_{-\infty}^{\infty} e^{ikt} X(t) dt, \tag{2.1}$$

which can be rightly recognized as the Fourier transform of $X(t)$. Due to this, characteristic functions carry over some of the useful properties of Fourier transforms, such as converting convolutions and derivatives to multiplications. The characteristic function $\tilde{X}(k)$ also completely describes the distribution $X(t)$, allowing for mathematical analysis of distributions that lack analytic expressions in real space – a feature that will become important in the following sections.

Lemons provides a proof [16] for independent identically distributed (i.i.d.) variables that is illustrative. Consider a random variable x_i drawn from a distribution $X(t)$ with zero mean and unit variance, or shift and scale a distribution to achieve this with no loss of generality. Take $s_n = x_1 + x_2 + \cdots + x_n$ as the sum of n such variables and S_n to be its distribution, the CLT can be written explicitly:

$$\lim_{n \to \infty} \frac{S_n}{\sqrt{n}} = N(0, 1), \tag{2.2}$$

where $\sqrt{n}$ is the standard deviation of the sum, and $N(0, 1)$ is the standard normal distribution (i.e. a Gaussian with zero average and unit standard deviation). The distribution of the sum of two random variables is a convolution, $S_2 = \int_{-\infty}^{\infty} X(t)X(t - \tau)d\tau$, and hence a product of their characteristic functions. The distribution of $S_n/\sqrt{n}$ can then be succinctly expressed by its characteristic function,

$$\tilde{S}_n(k) = \prod_{i=1}^{n} \mathbb{E}[e^{ikX_i/\sqrt{n}}] = \mathbb{E}[e^{ikX/\sqrt{n}}]^n. \tag{2.3}$$

Provided the moments of X exist, this can be expanded in a Taylor series:

$$\mathbb{E}[e^{ikX/\sqrt{n}}]^n = \mathbb{E}\left[1 + i\frac{k}{\sqrt{n}}X - \frac{k^2}{2n}X^2 + o\left(\frac{k^2}{2n}\right)\right]^n = \left(1 - \frac{k^2}{2n} + o\left(\frac{k^2}{2n}\right)\right)^n, \tag{2.4}$$

for which in the large n limit the higher order terms can be neglected. It can then be immediately identified with the expansion of $\exp[-k^2/2n]^n = \exp[-k^2/2]$ in the same large n limit

5

– the characteristic function of $N(0, 1)$. Note that no assumptions are made about the shape of the distribution. It should be clear that as long as the first moment ($\mathbb{E}[X]$) disappears then *any* sum of well behaved inputs will have leading order behavior of a Gaussian. The main requirements are only the independence of the input random variables and finiteness of the moments.

Because the CLT leads to a quasi-universal limiting distribution, many systems can be conceptualized as particles undergoing Gaussian kicks. Often these kicks represent the thermal jostling a particle experiences from the media which lead to Brownian motion. Because of the features of equilibrium, over a long time, the particle will visit all points in the space according to the Boltzmann distribution. There are many contexts, however, that are emphatically non-equilibrium. In particular, systems that transport energy or continually produce entropy may attain, at best, a steady state. Such systems have been found to exhibit non-Gaussian noise with infinite variance. With such extreme and erratic noise, the assumptions of equilibrium are no longer tenable.

The last statement deserves some digression. In practice one will never observe infinity, so what does this noise 'look' like? An insightful example that was described by Gull [17] is presented in Fig. 2.1. The problem described is thus: imagine a lighthouse that is a unit distance from the coast at unknown location x_0. The lighthouse emits directional flashes randomly according to the flat distribution $[0, 2\pi]$, which are detected at the coast. Only the position and not the incident angle of the flashes are recorded. What is the location of the lighthouse? Flashes close to parallel will lead to wildly divergent positions on the coast - the resultant distribution of flashes is not a Gaussian, it is the Cauchy distribution $1/(1+(x+x_0)^2)$. What the experimentalist quickly realizes upon measurement is that mean, $\langle x \rangle$, and variance, $\langle x^2 \rangle$, are not 'well behaved', as depicted in the bottom half of Fig. 2.1.

If one waits long enough, one will see a deviation so large that it overwhelms all previous measurements. Mathematically, the mean does not converge in the $n \to \infty$ limit. Because of this, one cannot estimate the center of the distribution quickly or easily via the mean as with
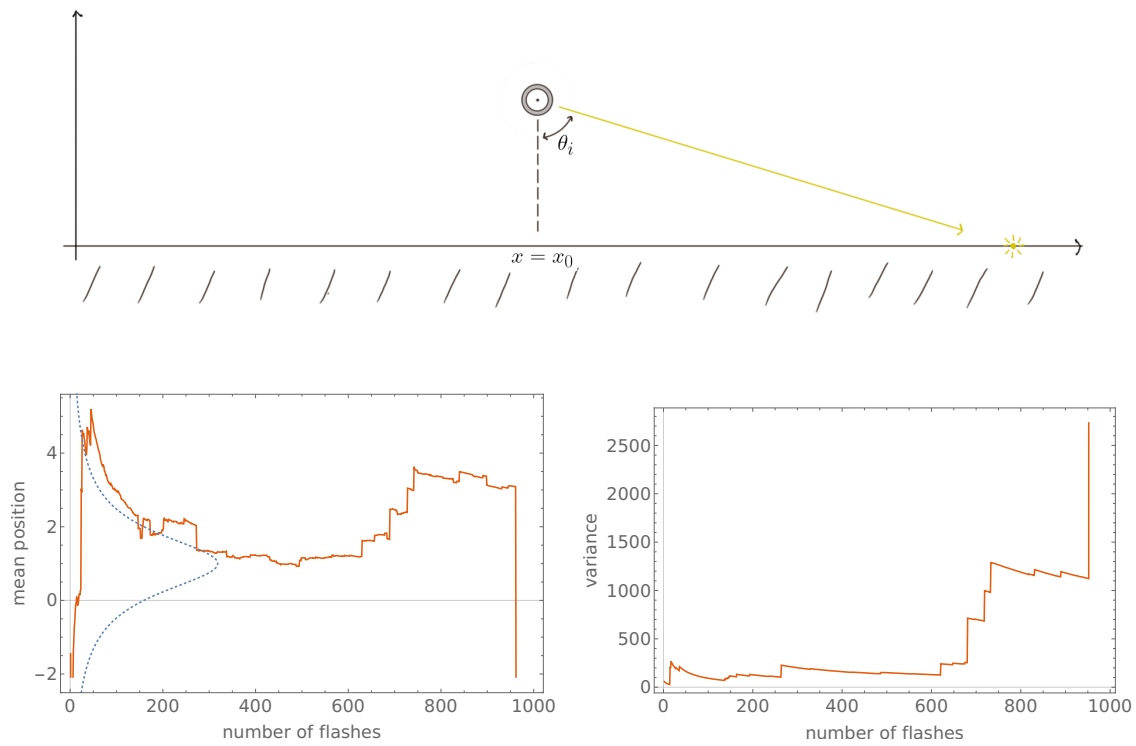
Figure 2.1: Gull's Lighthouse problem. A lighthouse emits light pulses in random directions θ_i that are detected on the coast (top), i.e. the x-axis. The resultant running mean position (bottom left) and running variance (bottom right) show erratic behavior. The dashed curve represents the actual probability density of flashes around the true position $x_0 = 1$.

the Gaussian. Neither will convergence be seen in the variance. It is therefore possible to observe the effects of an random variable with infinite variance, but this does not completely negate the criticism about infinities. After all, there are no infinite coastlines. However, as Mandelbrot points out in [18], there is utility in assuming these distributions to hold even when one knows the variance must be finite (but possibly large) much like it is useful to the photographer to assume the object of picture lies at infinity. Doing so preserves the simplicity and scaling behavior of distributions like the Cauchy.

Much of this behavior will occur throughout this chapter. First, however, the situation at equilibrium will be detailed along with a brief overview of a simple one-particle system and stochastic Langevin equation describing it. Then the consequences of non-Gaussian inputs will be investigated along with necessary modifications to the Langevin equation. A discretization of that modified Langevin equation is given that supports simulation and demonstrates the breaking of time-reversal symmetry. It will be shown below how this manifests in the moment to moment statistics of a time series, resulting in a quasi order parameter. It is shown how a Fokker-Planck equation can be used to generate the steady state distributions of this system. Finally, it will be demonstrated how this symmetry breaking can be used to analyze real-world data.

2.1.1   The Gaussian Assumption

A system subject only to Gaussian noise will eventually reach such an equilibrium distribution. It is useful to know in advance what the eventual equilibrium state of a system will eventually look like directly. This is quite easily obtained as the Boltzmann distribution. The Boltzmann distribution is a general statistical consequence of a 'lack of preference' for how the energy within a system is distributed among its parts, i.e. allowing every possible configuration to occur with equal probability. It turns out that configurations close to the Boltzmann distribution have greater representation, a greater number of microstates, by such an overwhelming margin that, at least for very large systems, they are the only states
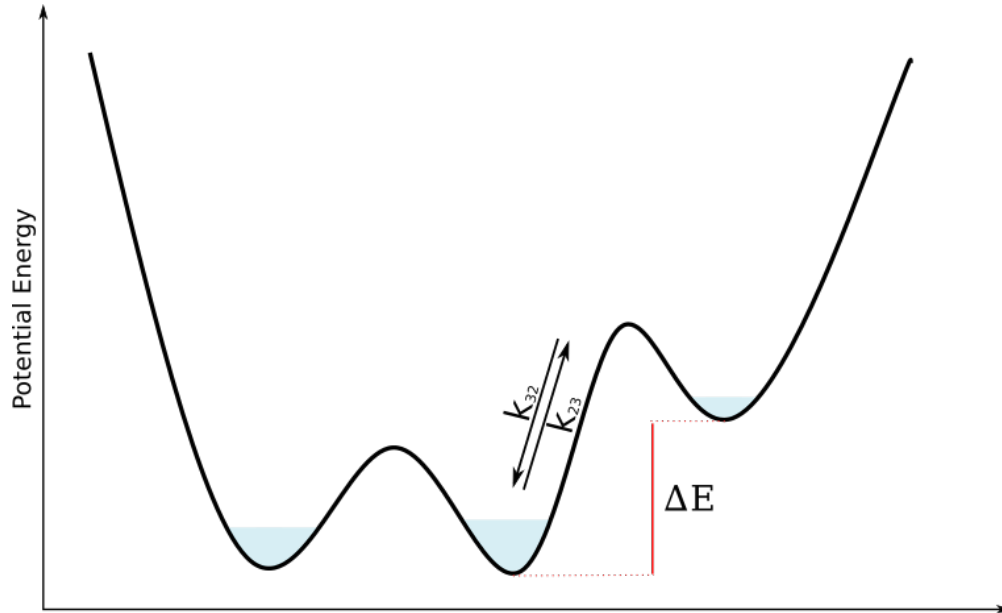
Figure 2.2: An arbitrary potential energy landscape.

one will ever find.

The eventual result is that the probability for a particular element of the system to be in a particular state is dependent on the energy, E, of that state as $\exp[-E/k_BT]$ [19]. Higher energy states are rarer because they leave less options (less energy) for configuring the rest of the system. The temperature, T, appears because each energy level becomes less significant as the total energy available to be distributed increases. To be more explicit, consider Fig. 2.2, which shows an arbitrary energy landscape inhabited by a large number of particles. Assuming equilibrium conditions and similar curvature (or discrete states), then, the relative number of particles between the second and third states is given by the *Boltzmann Factor*, $n_2/n_3 = \exp\left[\frac{\Delta E}{k_BT}\right]$, which is only a function of the temperature, the difference between the energy levels, and *nothing else*. That is quite a statement, as we are in principle free to make the rest of the landscape look however we wish.

Suppose we want to know how the particles arrange themselves within an individual well in Fig. 2.2. Provided the shape of the potential is known, there is no problem; one can just insert the expression for E into $\exp[-E/k_BT]$. Such exact knowledge is unlikely to be the case for an arbitrary system in nature. There are, however, reasonable approximations to

be made. Assume $f(x)$ describes the shape of the well. Close to the bottom, $x = x_0$, an expansion will have the form $f(x) \approx f(x_0) + \frac{f''(x_0)}{2}(x - x_0)^2$ where $f''(x_0)$ will necessarily be positive. The odd terms are neglected because of the relative local symmetry with the first odd term vanishing explicitly as $f'(x_0) = 0$. Higher orders, e.g. $(x - x_0)^4, (x - x_0)^6, ...,$ also vanish by virtue of restricting ourselves to the region near $x = x_0$. This means that in the vicinity of the bottom of a well there is a relatively universal quadratic behavior. This will be the focus below. And since $f(x_0)$ is just the energy level of the bottom of the well, it is straightforward to see that the resultant equilibrium distribution is Gaussian: $p(x) \propto \exp[-C(x - x_0)^2/k_B T]$ where $C > 0$ is a constant.

This still falls short of a complete description as it provides no information on how a system might *reach* this final equilibrium state. One method at our disposal is to follow the individual particles of a system in time. The Langevin equation,

$$m\frac{\mathrm{d}\dot{x}}{\mathrm{d}t} = -\lambda\dot{x} + \sigma\xi_\alpha(t), \tag{2.5}$$

describes a single particle subject to frictional forces proportional to λ and driven by the noise term $\xi_\alpha(t)$ with amplitude σ, where the subscript α has been added for consistency later. This equation is widely used to simulate trajectories in microscopic environments in lieu of simulating every atom of a media itself. The noise term represents the random 'kicks' a particle receives from thermal collisions, and thus scales with temperature. This approach invites some additional modifications, but the first consideration must be the form of $\xi_\alpha(t)$.

This is connected to a second important consequence of the equilibrium distribution, known as *microscopic reversibility*. This principle, introduced first by Boltzmann and popularized by Onsager [20, 21], states that reversing the time dimension for a system of particles will not change the distribution of collisions if the system is at equilibrium. This principle leads to the conclusion that every possible route between two states must be trafficked equally in both directions. In Fig. 2.2, this not only implies that $P_2 k_{23} = P_3 k_{32}$, but also
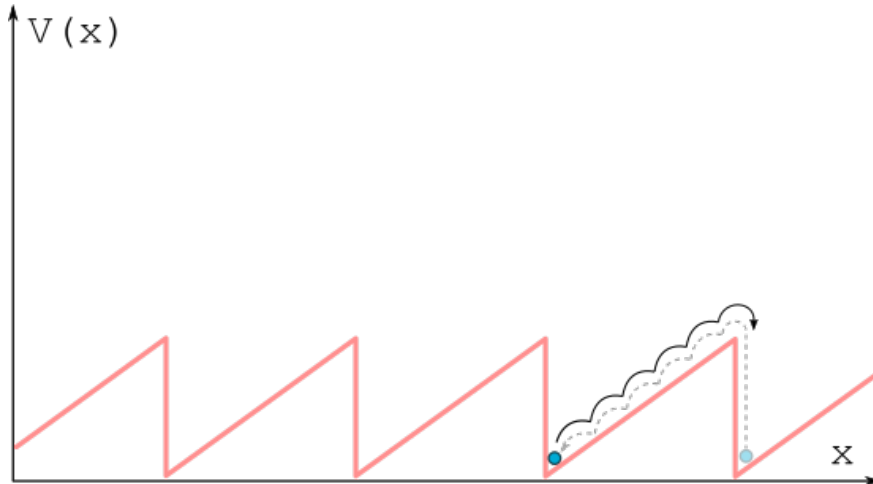
Figure 2.3: A Brownian particle in a ratchet potential with two mirrored trajectories.

that the time direction cannot be determined by inspecting individual trajectories between the states. This is crucial to maintaining the thermodynamic implications of equilibrium.

One insightful example of the consequences are the Brownian ratchets (Fig. 2.3), in which particles in a cleverly crafted potential receive repeated velocity 'kicks' drawn from a normal distribution. It may appear at first that the landscape lends itself to a net motion in one direction - that it is easier for noise to jostle particles up the gentle slope than launch them over the cliff - but this cannot be the case for equilibrium as this would, in essence, create a perpetuum mobile with particles spontaneously flowing to the right. It turns out that for Gaussian noise, the most likely trajectories in each direction are exact reversals of each other [22, 23, 24]. By the arguments of the last paragraph, of course, it could not be any other way. This is, however, a strong affirmation that noise at equilibrium is indeed Gaussian.

This makes sense in light of the central limit theorem (CLT). Convergence is very good for even a small number of inputs n in Eq. 2.2 and even faster if those inputs are already similar in distribution to a Gaussian themselves. In contrast to the requirements above for equilibrium itself, this is a veritable triviality in many familiar contexts - atoms and molecules, for instance, can interact more than a trillion times per second and each of those interactions are themselves the consequence of trillions of interactions. As a result, much of

the randomness of nature - the noise - takes on exactly the same form - the Gaussian.

At timescales much larger than picoseconds, inertia becomes irrelevant and particles can be assumed to reach their terminal speeds "instantaneously" upon application of a force. This is known as the overdamped limit. The left hand side of the Langevin equation is set to zero and what remains is the triviality of the particle velocity being random. In practice, one usually adds at least a second component: a physically relevant potential. This yields:

$$\lambda \dot{x} = \sigma \xi_\alpha(t) - \mathrm{d}V(x)/\mathrm{d}x, \tag{2.6}$$

in which the additional term $\mathrm{d}V(x)/\mathrm{d}x$ represents the force created by the potential. This equation also provides the means to observe the process via simulation, which will be described later. Importantly, when simulating, there is no restriction on the noise term $\xi_\alpha(t)$ - any distribution can be drawn from, Gaussian or non-Gaussian.

2.1.2 Deviation: Levy Noise

The normal distribution is not the only limiting distribution described by the central limit theorem. Loosening the restriction of finite moments on the random inputs leads to the so called alpha-stable or Lévy distributions [25]. Infinite variance leads to 'fat' tails in the distribution representing heightened frequency of extreme events. It is easy to understand that if there is even one stochastic input with such a tail in a sum, then that sum will retain that tail and infinite variance (though it may be scaled). Except for special cases, the symmetric variants of these limiting distributions are best described by their characteristic function:

$$\tilde{p}_\alpha(k) = \exp[ik\mu - |\sigma k|^\alpha] \tag{2.7}$$

for position parameter μ and scale parameter σ. The $0 < \alpha < 2$ is often referred to as the stability index or tail parameter and describes how quickly the probability density decreases far from the mean. The σ is the same noise amplitude which appears in Eq. 2.6.
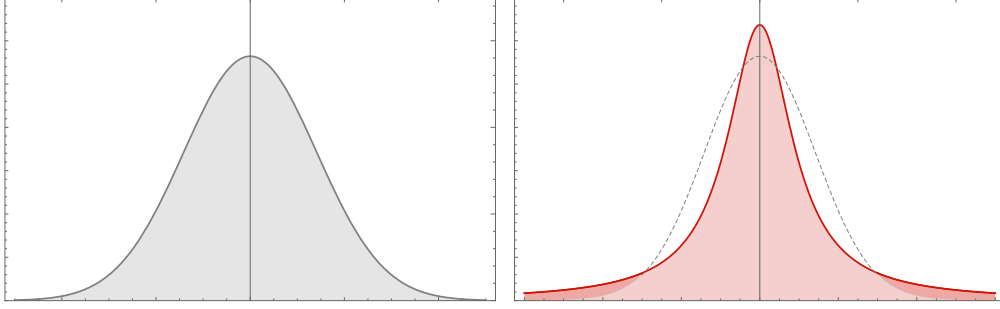
Figure 2.4: A Gaussian distribution ($\alpha = 2$, left) and the Cauchy distribution ($\alpha = 1$, right). The additional tail area of the Cauchy distribution is darkened.

Taking the Fourier transform allows one to retrieve the probability density function, however analytic expressions only exist for special cases. Two of these are shown in Fig. 2.4. Setting $\alpha = 2$ yields a Gaussian with standard deviation $\sqrt{2}\sigma$, and setting $\alpha = 1$ yields the Cauchy distribution. The Cauchy distribution with its power-law tails is representative of the alpha-stable distributions. From Eq. 2.7 the asymptotic behavior can be derived [25]:

$$ p_\alpha(z) \sim \frac{\sigma^\alpha \sin(\pi\alpha/2)\Gamma(\alpha+1)}{\pi} \frac{1}{|z|^{\alpha+1}} \text{ as } |z| \to \infty, \tag{2.8} $$

where $\Gamma(.)$ denotes the gamma function. The leading ratio is just a constant while $1/|z|^{\alpha+1}$ is descriptive of behavior that is phenomenologically different from a Gaussian. The darkened area in the right side of Fig. 2.4 displays these tails that persist even as the Gaussian distribution falls off exponentially. These power-law tails are what produce interesting behavior in systems - a prevalence of large events and power-law scaling - but the concomitant infinite variance often makes these distributions difficult to work with analytically.

Over the last few decades it has become ever more clear that Lévy distributions are more than just a mathematical construct. In 1963 Mandelbrot found that the day-to-day changes of the prices of cotton stocks followed a Lévy distribution with $\alpha = 1.7$ [18, 26]. In 1993 Peng et al noticed that time intervals between subsequent heartbeats are also Lévy distributed [27]. Lévy distributions have been identified in solar physics [28], in climate data [29], plasma turbulence [30], etc. Very recently simulations and theoretical analysis showed that a tracer

particle in a solution with active microscopic swimmers exhibits displacements with a power-law tail [31]. The common denominator for systems that exhibit Lévy distributions appears to be the nonequilibrium nature of these systems. Noise with a fat, power-law tail and the corresponding "extreme events" appear to be inherent to systems that convert, transport, and/or dissipate energy.

While microscopic reversibility still applies to a Lévy noise driven particle in free space, it can be violated if there is a potential. This is demonstrated in Fig. 2.5, which shows trajectories of a simulated Brownian particle in a quadratic potential (cf. Fig. 2.5a). The first trajectory involves Gaussian noise and the second Lévy noise with $\alpha = 1.2$. Even though the potential imposes correlations onto the eventual signal, there are no features in Fig. 2.5b to hint at the forward direction in time. Of course this must be so, as explained in the previous section. For Lévy noise the situation is different; large spikes can be seen followed by a prolonged sliding down towards the bottom of the well. As with Gaussian noise, the most likely trajectory to travel from a point A high on the potential to a lower point B is a deterministic downslide of all size zero kicks. Unlike with Gaussian noise, the most likely trajectory upwards from B to A for the Lévy case is a single jump. This breaking of time reversal symmetry becomes more extreme as the α parameter moves away from $\alpha = 2$ and provides one way to quantify the distance from equilibrium. This is the subject of Section 2.4.2.

This has implications for systems which are asymmetric. Reconsider the situation of Fig. 2.3. For Lévy noise it has been shown that there is actually a net flow (leftward as drawn) in the system [32]. For large kicks the force of the potential is less important than the spatial distance between two adjacent wells. Since the majority of particles still reside near the bottom of the potentials, transitions over barriers to the left can more easily happen in a single large kick. Then, since these large kicks are 'rare' for individual particles, it is likely that, once beyond the barrier, the particle will deterministically slide to the bottom of the well that kick has brought it to.
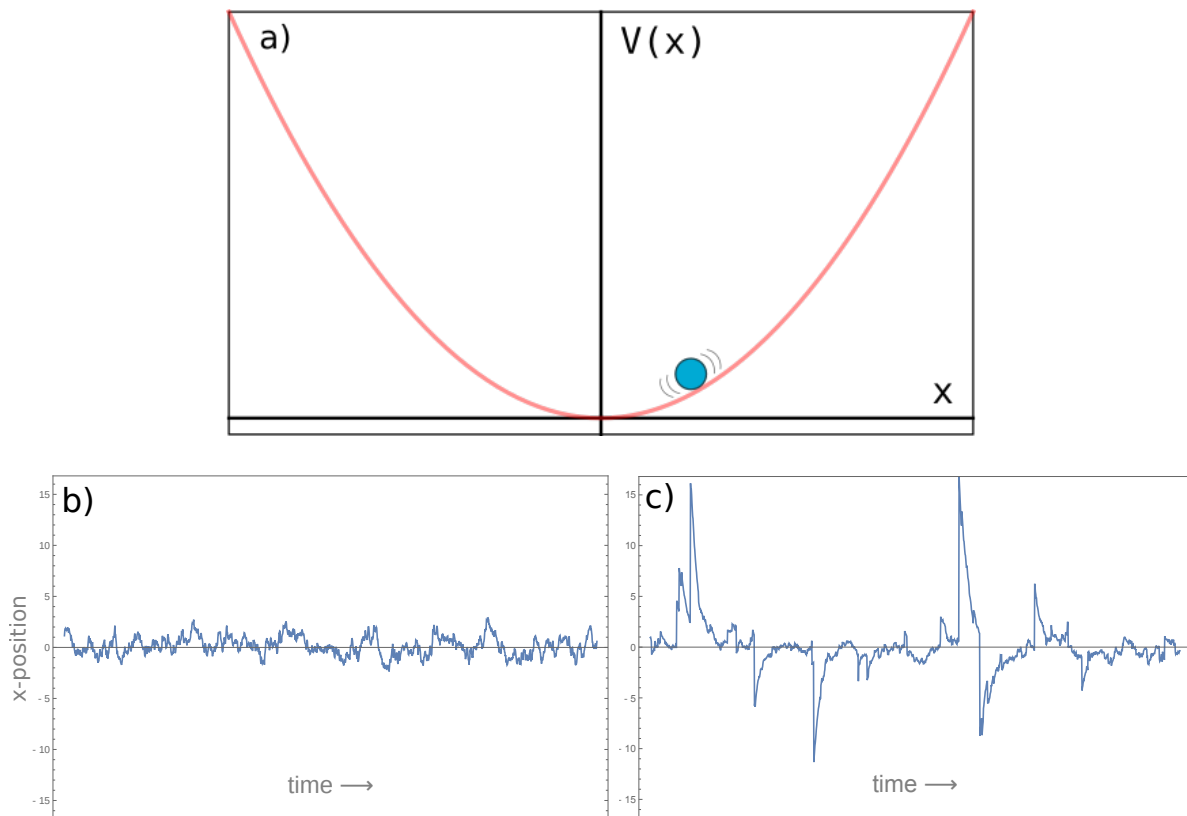
Figure 2.5: a) A Brownian particle in a well. b) Sample position time series when driven by Gaussian noise. c) Sample position time series when driven by Lévy noise.

2.2 Solving Overdamped Stochastic Systems

2.2.1 Langevin Simulations

It has become common practice to pair analysis of stochastic systems with computer simulations for the sake of rigor. The results of long or complex mathematical analyses can often be reproduced by model systems that follow a set of relatively simple rules. Such simulations also add credibility to any assumptions or approximations that may have been made in the course of a derivation – or at least replace them with more generally accepted assumptions and approximations. Despite the relative simplicity, it is in some sense important to understand where Langevin simulations stand in that regard.

As was already mentioned in Sec. 2.1.1 trajectories of constituent particles of a stochastic system can be described via the Langevin equation $md\dot{x}/dt = -\lambda\dot{x} + \sigma\xi_\alpha(t)$ (Eq. 2.6). Here inertia has been reintroduced to Eq. 2.6 by replacing the potential term $dV(x)/dx$ with $md\dot{x}/dt$. This equation of just three terms contains only the resultant acceleration md^2x/dt^2, friction (damping) force $\lambda\dot{x}$, and stochastic force $\sigma\xi_\alpha$ with the σ coefficient representing a scale factor that usually depends on some macroscopic quantity like temperature. The average behavior or time evolution of a system can be characterized by repeatedly applying this equation over many iterations until the desired accuracy is achieved.

It should be clear that this represents something of a gross simplification for most physical systems. Consider the simple case of massive molecules diffusing in water, i.e. Brownian motion. A single Langevin equation can perfectly well describe the motion of the massive molecule while omitting any accounting of collisions between solute molecules or any description of local interactions. These effects can of course be included, leading one from Langevin dynamics to molecular dynamics, but there is a concomitant computational cost. Most molecular dynamics simulations operate with total lengths of nanoseconds.

The starting assumption that leads to the simplicity of Eq. 2.6 is that any function in the phase space of a system may be decomposed into quickly and slowly varying orthogonal

components [33]. 'Fast' components in this context are not different than those referenced in the definition of local equilibrium, e.g. the thermalization of solute molecules. So long as one considers time steps of a scale much larger than these processes play out, their effects on particles of interest can be consolidated into the single stochastic term ξ_α. By the arguments of Sec. 2.1 this often is taken as Gaussian white noise but other choices such as correlated or alpha stable noise are legitimate.

Noise Generation

Sampling a random variable from a known distribution is a relatively straightforward process. The cumulative density function (CDF) of a random variable X can be obtained by integration of its probability density function, $\mathrm{CDF}_X(x) = \int_{-\infty}^{x} P(t)dt$. The CDF has a range $[0, 1]$ and describes the probability that a random draw is smaller than x, i.e. $\mathrm{CDF}_X(x) = P(X \leq x)$. Thus, the inverse of this function can be used to map random numbers from the unit interval $[0, 1]$ back onto the distribution of interest. Many specific distributions have more refined algorithms that are much more efficient. The Box-Muller transform was created in the 1950s [34] and generates pairs of independent normally distributed numbers from a pair of independent random numbers U_1, U_2 from the uniform distribution on the square unit interval:

$$x_1 = (-2\ln U_1)^{1/2} \cos(2\pi U_2) \tag{2.9}$$

$$x_2 = (-2\ln U_1)^{1/2} \sin(2\pi U_2). \tag{2.10}$$

For the alpha stable variables that will be of interest it is more complicated. Only a complicated series representation is available for the stable distributions [35], so taking the inverse function of the CDF first requires numerical evaluation of the Fourier transform of the characteristic function (Eq. 2.7) for the specific parameters of interest. A method was, however, developed that can relatively efficiently convert two random numbers into a single random number with the same distribution as a stable distribution with stability

parameter α and skew parameter β - β will be taken to be 0 throughout this work. The Chambers-Mallows-Stuck method [36, 37] for random input numbers U_1, E_1 gives:

$$X(\alpha, \beta) = \frac{\sin \alpha(U_1 - \Phi)}{(\cos U_1)^{1/\alpha}} \left(\frac{\cos(U_1 - \alpha(U_1 - \Phi))}{E_1} \right)^{(1-\alpha)/\alpha}, \alpha \neq 1, \tag{2.11}$$

$$X(1, \beta) = \frac{2}{\pi} \left((\frac{\pi}{2} + \beta U_1) \tan(U_1) - \beta \left(\frac{\frac{\pi}{2} E_1 \cos U_1}{\frac{\pi}{2} + \beta U_1} \right) \right), \tag{2.12}$$

where U_1 is uniformly distributed on $(-\pi/2, \pi/2)$, E_1 is from the exponential distribution e^{-x} and $\Phi = -\frac{\pi}{2}\beta(1 - |1 - \alpha|)/\alpha$. Despite the seeming complexity, Eq. 2.11 is composed of relatively simple functions and has become the primary method for the generation of alpha stable random numbers. It is included in the standard *Mathematica* installation and there are packages available for other languages ([38] in *MATLAB*, for example).

Notice that Eq. 2.11 has no provision for the location parameter μ or the scale parameter σ. Adjusting the location is trivial and will be taken as $\mu = 0$ throughout in any case. The scale parameter will require some special attention.

Discretization and Scaling

In computer simulations time usually advances in discrete uniform 'steps'. Eq. 2.6 describes a continuous process and must first be discretized to describe the evolution of a particle in a series of small steps of time (Δt). The discretized form of Eq. 2.6 is

$$x_{n+1} = x_n - \frac{dV(x_n)}{dx}\Delta t + (\Delta t)^{1/\alpha}\theta_{\alpha,i}, \tag{2.13}$$

where the friction coefficient λ has been absorbed into the timescale and noise amplitude by taking $t = t'/\lambda$ and $\sigma = \sigma'/\lambda^{\alpha}$. $\theta_{\alpha,i}$ represents a draw from an alpha stable distribution with unit scale, no skew, and stability parameter α. This is known as the forward Euler method of discretization due to the approximation of the potential as linear (Euler) from the point before the timestep (forward), i.e. using $V(x_n)$ rather than $V(x_{n+1})$. The $(\Delta t)^{1/\alpha}$ emerges to maintain scaling. The effect of many small timesteps must accumulate to an

equivalent single large timestep; a property referred to as 'stability under addition' [39]. In the Gaussian case this follows directly from the mean displacement of $\sqrt{2Dt}$ for diffusion coefficient $[D] = \text{length}^2/\text{time}$ or can be seen equivalently from the convolution of standard normal Gaussians – $N_1(x) \otimes \ldots \otimes N_n(x) = \mathcal{F}^{-1}((\sqrt{2\pi})^{n-1}N(k)^n) = \exp[-x^2/4n]/\sqrt{n}$.

For general α the argument requires more care. When a stochastic variable ζ is multiplied with a factor γ ($\gamma > 1$), the distribution for $\zeta' = \gamma\zeta$ is wider and has a scale factor (or standard deviation) that is γ times larger. How the probability distributions $p(\zeta)$ and $p'(\zeta')$ are related is easily derived from $p'(\zeta')\,d\zeta' = p(\zeta)\,d\zeta$. We find:

$$p'(\zeta') = (1/\gamma)\,p(\zeta'/\gamma). \tag{2.14}$$

This result makes sense after the realization that the horizontal stretching by a factor γ (the dividing by γ in the argument) must be accompanied by a vertical compression (the $1/\gamma$ prefactor) to maintain normalization.

For $k \to 0$ the characteristic function $\tilde{p}_\alpha(k) = \exp\left[-\sigma^\alpha|k|^\alpha\right]$ (cf. Eq. (2.7)) can be approximated by:

$$\tilde{p}_\alpha(k) \approx 1 - \sigma^\alpha|k|^\alpha. \tag{2.15}$$

The probability distribution $p_\alpha(z)$ is related to the characteristic function $\tilde{p}_\alpha(k)$ through $p_\alpha(z) = \frac{1}{2\pi}\int_{-\infty}^{\infty} \tilde{p}_\alpha(k)\exp\left[-ikz\right]\,dk$. For $k \to 0$ the product kz in the exponent will only differ significantly from zero if $z \to \infty$. It is therefore that the $k \to 0$ limit corresponds to the $z \to \infty$ limit. The second term in Eq. (2.15) readily leads to the power law Eq. (2.8) through the Fourier transform.

Consider an overdamped free particle. When subject to Lévy noise, the particle's motion is described by $\dot{x} = \sigma\xi_\alpha(t)$. The Lévy noise term, $\xi_\alpha(t)$, has structure on all scales. Because of this, the discrete timesteps Δt that are necessary for a simulation include a scale factor for $\xi_\alpha(t)$ that depends on Δt. We have $\xi_\alpha(t_i)\,\Delta t = \theta_{\alpha,i}(\Delta t)^{1/\alpha}$, i.e. $\xi_\alpha(t_i) = \theta_{\alpha,i}(\Delta t)^{(1-\alpha)/\alpha}$. Here $\theta_{\alpha,i}$ denotes the i-th random number drawn from a zero-centered, symmetric Lévy

distribution with stability index α and unity scale parameter. It is obvious from here that the amplitude $(\Delta t)^{1/\alpha}$ is like the scale factor γ.

For an α-stable distribution with a unity scale factor we have for large $|\theta|$:

$$p_\alpha(\theta) \sim \frac{\sin\left(\frac{\pi\alpha}{2}\right)\alpha\Gamma(\alpha)}{\pi}\frac{1}{|\theta|^{\alpha+1}} \quad \text{as } |\theta| \to \infty. \tag{2.16}$$

In a simulation with a timestep Δt, we have $\kappa_\alpha(t_i) = \xi_\alpha(t_i)\Delta t = \theta_{\alpha,i}(\Delta t)^{1/\alpha}$ for the random kicks. Realizing that $\Delta t^{1/\alpha}$ is the scale factor that connects $\kappa_\alpha(t_i)$ and $\theta_{\alpha,i}$, and next applying the result that was derived above, the asymptotic behavior of the distribution (analogous to Eq. 2.8) $p_\alpha(\kappa)$:

$$p_\alpha(\kappa) \sim \frac{\Delta t \sin\left(\frac{\pi\alpha}{2}\right)\alpha\Gamma(\alpha)}{\pi}\frac{1}{|\kappa|^{\alpha+1}} \quad \text{as } |\kappa| \to \infty. \tag{2.17}$$

This implies that the term σ^α in Eq. (2.8) has the same effect on the stochastic input as Δt, i.e. the characteristic function for this input is $\tilde{p}_\alpha(k) = \exp[-\sigma^\alpha\Delta t|k|^\alpha]$. One then has for the continuous and discretized Langevin equations:

$$\dot{x} = \sigma\xi_\alpha(t) \tag{2.18}$$

$$\Delta x = \sigma\Delta t^{1/\alpha}\theta_{\alpha,i}. \tag{2.19}$$

2.2.2 Fokker-Planck Representation

The diffusion process described by Eq. 2.6 is a Markov process. A master equation describes the evolution of such a system and is traditionally formulated in discrete form [40]:

$$P(x_n, t_i + 1) = \sum_{m=1}^{N}\left(P(x_m, t_i)W(x_m, x_n) - P(x_n, t_i)W(x_n, x_m)\right). \tag{2.20}$$

Here $P(x_n, t_i)$ represents the probability to be in state x_n at time t_i and $W(x_n, x_m)$ represents the probability to transition from state x_n to state x_m per unit of time. Thus the master equation can be seen as a simple accounting of particles entering from each state

(the first term) and all the particles exiting to other states (the second term). Any external 'potential' is manifested implicitly in the transition rates. Note that this Markov description is deterministic – given the initial state $P(x,0)$ one can determine the probability density for all further points in time.

Eq. 2.20 has a continuous time counterpart. If the time and position dependence of jump lengths are independent, it has the form [33],

$$\frac{\partial P(x,t)}{\partial t} = \int_0^t dt' \Phi(t - t') \int dx' \left[W(x, x - x')P(x', t) - W(x', x - x')P(x, t) \right], \quad (2.21)$$

which includes a memory parameter Φ and the transition probabilities W are now functions of kick size $x - x'$ instead of defined per state. The second integral serves the same function as before and integrates the inflow to position x from elsewhere in the region. This describes a much more general situation than the Langevin Eq. 2.6 which contains no information about W. Eq. 2.6 contains a stochastic force term with several assumptions. These assumptions can be applied to the master equation to create an equivalent deterministic equation.

The memory kernel Φ allows for the system's history to be taken into account and often, but not necessarily, takes an exponential form. But for the Langevin setup described in Sec. 2.1.1 the thermal jostling represented by the stochastic term is assumed to be uncorrelated in time. This is also referred to as instantaneously correlated because the memory kernel takes the form of a delta function: $\int_0^t dt' \delta(t - t') = 1$.

The remainder of Eq. 2.21 can be expressed as a Taylor expansion in x, known as the Kramers-Moyal expansion [41]:

$$\frac{\partial P(x,t)}{\partial t} = \sum_{n=1}^{\infty} \frac{(-1)^n}{n!} \frac{\partial^n}{\partial x^n} \left[P(x,t) \int_{-\infty}^{\infty} (x - x')^n W(x, x - x') dx \right]. \quad (2.22)$$

Keeping just the first two terms, we can write this as:

$$\frac{\partial P(x,t)}{\partial t} = -\frac{\partial}{\partial x} \left(\frac{\partial \langle x - x' \rangle}{\partial t} P(x,t) \right) + \frac{1}{2} \frac{\partial^2}{\partial x^2} \left(\frac{\partial \langle (x - x')^2 \rangle}{\partial t} P(x,t) \right). \quad (2.23)$$

21

The time derivatives appear because W describes a transition rate. Since the noise is already assumed to have mean zero, $\langle x - x' \rangle$ can be identified with drift, proportional by friction coefficient γ to the force of the potential $V'(x)$. The expectation value in the second term is just the mean-squared displacement. For Gaussian white noise we can take $\langle (x-x')^2 \rangle = 2Dt$. This leads directly to the Fokker-Planck (or Smoluchowski) equation:

$$\frac{\partial P(x,t)}{\partial t} = -\frac{1}{\gamma} \frac{\partial[V'(x)P(x,t)]}{\partial x} + D \frac{\partial^2 P(x,t)}{\partial x^2}. \tag{2.24}$$

Though the above derivation is standard, it is problematic for Lévy noise ($\alpha \neq 2$) as the key assumption in the continuum limit is that individual kicks are small to justify the Taylor expansion. This is reasonable for Gaussian noise, but large jumps are inherent to Lévy statistics and make an analogous derivation more difficult, though it can be done [42]. A more direct route from the Langevin can be taken by using the scaling property derived in the last section [43, 44]. This result was that the kick distribution has a characteristic function that scales with time like $\tilde{p}_\alpha(k) = \exp[-\Delta t |k|^\alpha]$. Recalling that this behavior was derived to maintain the scaling behavior of a sum of inputs, this expression can be identified as the characteristic function for a force-free Langevin particle after time Δt, i.e. $p(x, t = \Delta t) = \mathcal{F}^{-1}[\tilde{p}_\alpha(k)]$ where $\mathcal{F}^{-1}$ represents the inverse Fourier transform in space. Then we can reinsert the generalized diffusion constant D and taking the partial derivative w.r.t. time. Note that the independent variable for the Fourier transform was x, i.e. the *position*. The time derivative can still be taken as normal and yields:

$$\frac{\partial p(x,t)}{\partial t} = \mathcal{F}^{-1}[-D|k|^\alpha \exp[-tD|k|^\alpha]] = \mathcal{F}^{-1}[-D|k|^\alpha \tilde{p}(k)]. \tag{2.25}$$

Here a noninteger power of k is involved. This requires introduction of the Riesz fractional derivative [40]:

$$\mathcal{F}\left[\frac{\partial^\alpha u}{\partial |x|^\alpha}\right](k) = -|k|^\alpha \mathcal{F}[u](k). \tag{2.26}$$

22

The Riesz derivative merely extends to fractional order a very useful property of the Fourier transform - that a derivative with respect to the independent variable becomes a multiplication with the transformed variable in Fourier space. Utilizing Eq. 2.26 in Eq. 2.25 yields the fractional Fokker-Planck equation (FFPE) with no external force:

$$\frac{\partial p(x,t)}{\partial t} = D\frac{\partial^\alpha p(x,t)}{\partial |x|^\alpha}, \tag{2.27}$$

where D has dimensions of length$^\alpha$/time and is thus different from the standard diffusion coefficient. From here there are several ways to extend the case to include a known potential $V(x)$ [45], but one of the most widely used is as a drift proportional to the force:

$$\frac{\partial p(x,t)}{\partial t} = -\frac{\partial}{\partial x}\left[\frac{V'(x)p(x,t)}{\lambda m}\right] + D\frac{\partial^\alpha p(x,t)}{\partial |x|^\alpha}, \tag{2.28}$$

which is the full FFPE with friction coefficient λ and particle mass m. This correctly reduces to Eq. 2.24 with $\alpha = 2$ and the relation $\langle x^2(t)\rangle = 2Dt$ as $\langle x^2(t)\rangle$ is just the second moment of the normal distribution $\mathcal{N}(0, t^{1/2})$.

Equation 2.28 describes the evolution of a system with Lévy noise and can in principle be used to solve for the steady state of such a system by equating the right hand side to zero. The fractional derivative poses the primary challenge. Since it is also defined by its Fourier transform, not unlike the alpha stable distributions, full analytic solutions are only possible in limited circumstances. Some of these will be discussed in further sections (Sec. 2.4.1 & 3.3). There are, however, representations of the fractional derivative in real space that allow for some manipulation.

The reason the fractional derivative leads to difficult and complicated expressions is that it is not a 'local' operator. There are actually many definitions for calculating fractional derivatives [46], but what they have in common is that the fractional part of the derivative is computed via integration. For instance, the right and left handed Riemann-Liouville

fractional derivative of order α is:

$$D_{a+}^{\alpha} f(x) = \frac{1}{\Gamma(n-\alpha)} \frac{d^n}{dx^n} \int_a^x \frac{f(z)dz}{(x-z)^{\alpha-n+1}}, \tag{2.29}$$

$$D_{b-}^{\alpha} f(x) = \frac{(-1)^n}{\Gamma(n-\alpha)} \frac{d^n}{dx^n} \int_x^b \frac{f(z)dz}{(z-x)^{\alpha-n+1}}, \tag{2.30}$$

where n is the smallest integer greater than α. Here the function is first fractionally inte-grated, and that integration involves the entire domain $[a, b]$. Such definitions allow for the possibility of numerically following the FFPE forward in time on a mesh until a steady state is found [47, 48]. Because of the non-local nature of Eq. 2.29 this is not necessarily more computationally efficient than the much simpler Langevin approach.

2.3 'Unsolving' Stochastic Systems

The above sections deal with the modelling of idealized systems. It has been presupposed that such systems actually exist in the real world. However, the question of how to characterize a given system, or more likely a given data stream, remains. Two related issues will be discussed - common methods to estimate the noise parameters (e.g. α) and some methods to discriminate between types of random walks.

Parameter estimation

Different methods are available to estimate the parameters of the α-stable distribution that best fits a set of observed data [49, 50]. Often where one starts is with an estimation of the tail parameter, α. The most straightforward method is to take advantage of the power law behavior of the tail, e.g. Eq. 2.8. The empirical distribution (the set of 'noise values' from the data) should form a straight line on a log-log plot with slope $-\alpha$. Alternatively one can use the behavior of the mean squared deviation (MSD). Though the second moment for the stable distributions is in principle infinite for $\alpha < 2$, repeated estimates for a process should produce convergent behavior with increasing t.

The mean squared deviation can be derived from the aforementioned scaling relation Eq. 2.14[43]:

$$\langle x^2(t) \rangle \propto t^{2/\alpha}. \tag{2.31}$$

In other words, $MSD(X(t)) = (X(t) - X(0))^2$ should also yield a power law, but with the scaling exponent $2/\alpha$. More usually the MSD is averaged over a number of trajectories or, in the case of a single long trajectory, averaged by segmenting a single trajectory. In this case, the average MSD for a small time lag τ is:

$$M_N(\tau) = \frac{1}{N - \tau + 1} \sum_{k=0}^{N-\tau} (X_{k+\tau} - X_k)^2. \tag{2.32}$$

The quantile method of McCulloch [51] has also proven practical. Locating the five quantiles (5th, 25th, 50th, 75th, 95th) is as simple as ordering the data. McCulloch then provided a simple formula and a set of pre-tabulated results from which one could determine the α parameter and skew.

The maximum likelihood method is omnipresent in hypothesis testing and easy to understand [52]. It is also efficient enough for smaller sets of data and can be used to fit all parameters of the chosen distribution. It uses a general expression for independent and identically distributed (i.i.d.) variables, the log-likelihood [53]:

$$L(\xi) = \log \left(\prod_{i=1}^{n} f(X_i | \xi) \right) = \sum_{i=1}^{n} \log(f(X_i | \xi)), \tag{2.33}$$

where $f(X_i | \xi)$ represents the probability to have drawn value $X_i \in X_1, \ldots, X_n$ from the distribution ξ. Eq. 2.33 can then be maximized on the parameters of ξ. For the normal distribution, a relatively simple linear expression results. For the stable distributions in question, one generally has to resort to pre-calculated fits of the distribution density function.

Ultimately these methods and others face the same difficulties. Primarily they rely on the ability to separate the noise from the signal. Lévy noise is characteristically erratic,

making even estimating the mean of a data set challenging – indeed the mean of the stable distributions for $\alpha \leq 1$ is undefined. The tail method relies on extreme values which are naturally sparse. Finally there is often no guarantee that parameters such as the stability index α or diffusion constant do not change in time. Later in section 2.4.2 a method to estimate α that surmounts these problems in limited circumstances will be shown.

   Noise Processes

A number of different schemes have been developed to model anomalous diffusion. The major examples are based upon extensions or generalizations of the simple random walk – a particle that takes a unit step left or right each unit of time with equal probability. Allowing this step to have a variable length drawn from a Gaussian distribution yields the classic description of Brownian motion encapsulated by the basic overdamped Langevin equation $dx(t)/dt = \xi(t)$. If one allows $\xi(t)$ to be drawn from the more general alpha-stable distributions, one retrieves the Lévy flights described thus far.

If instead one keeps the Gaussian white noise for $\xi(t)$, but introduces random waiting times between steps, one has the continuous time random walks (CTRW). The waiting times, which originally represented particle trapping that occurs in semiconductors, are often drawn from power law distributions yielding subdiffusive behavior. And finally if one replaces the uncorrelated Gaussian noise $\xi(t)$ with correlated 'fractional' Gaussian noise ξ_{fGn}, one has the so-called fractional Brownian motion (FBM), or fractional Lévy stable motion (FLSM) in the case of fractional Lévy noise. In these cases, it is the correlations that are power-law distributed.

Each of these models produce somewhat distinct particle trajectories and it is not always clear when a particular description is most suitable. Fig. 2.6 shows some pronounced examples of their 1D versions. It is immediately apparent how the large jumps in Lévy flights or the long pauses in a CTRW can lead to super- or subdiffusion. More subtle is the tendency for the FBM to preserve its upward or downward trend. This tendency was brought to prominence by Harold Edwin Hurst during his engineering of the Aswan dam [54] and is
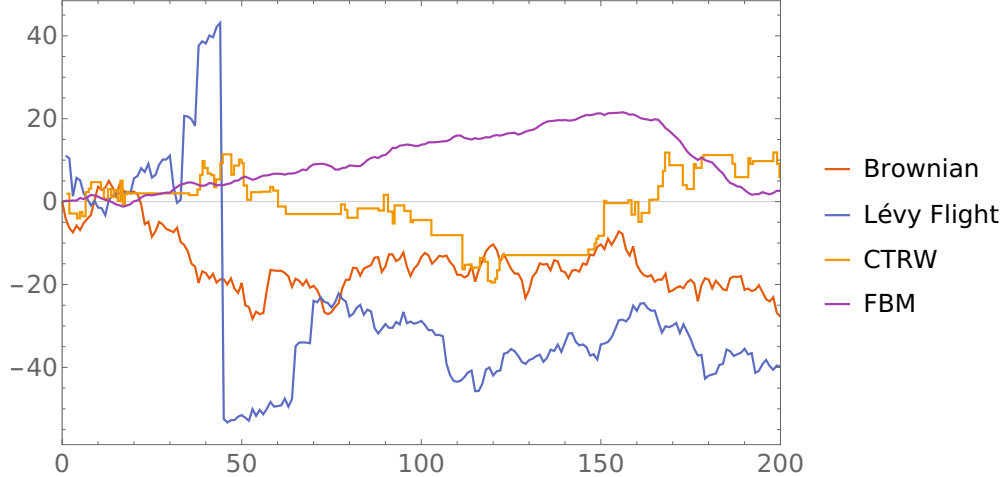
Figure 2.6: Comparison of common random walk models. For the Lévy flight $\alpha = 0.8$ and for the fractional Brownian motion the Hurst exponent $H = 0.9$

now commonly characterized by the Hurst exponent $0 \leq H \leq 1$. The volume of water in the reservoir behind a dam is an integration of flows from subsequent years. If the seasonal flows from the Nile river were i.i.d., one would find a random walk for the volume, but this is not what Hurst discovered. Instead of $\sqrt{\langle x^2 \rangle} \propto \sqrt{t}$ for the MSD, he found $\sqrt{\langle x^2 \rangle} \propto t^H$ with $H = 0.91$. $H > 0.5$ means that the MSD tends away from 0 *more* than it would for a purely random process. Subsequent data points (or river flows) have a positive correlation. The Hurst exponent of the FBM in Fig. 2.6 has the value $H = 0.9$ and is dominated by a long, smooth trend. $H < 0.5$ leads to anticorrelation and characteristically 'rough' time series.

The distinction between these processes will not necessarily be so clear as it is in Fig. 2.6. There are a few statistical tools which can be used to discriminate which may be most appropriate. A first option is the behavior of the MSD and $M_N(\tau)$. Ref [55] provides a table for the behavior of many of these processes and also points out the danger of naively assuming that $\langle MSD(x) \rangle = \lim_{\tau \to \infty} M_N(\tau)$ which is only true for some. For FBM and FLSM for instance, both go as t^{2H} (τ^{2H}) but for the CTRW $\langle MSD(x) \rangle \propto t^{2H}$ and $\langle M_N(\tau) \rangle \propto \tau t^{2H-1}$. Likewise for Lévy flights, the MSD is infinite, scaling as $t^{2/\alpha}$ (Eq. 2.31), but $\langle M_N(\tau) \rangle \propto \tau^{2/\alpha - 1}$.

Another method that has shown some promise for analyzing single trajectories is the p-variation, which can help distinguish between FBM and FLSM [56, 57]. FBM and FLSM generalize their respective classical counterparts to allow for time correlations between values, embodied by the Hurst Parameter H. The p-variational test can be seen as a way of probing these time correlations.

The p-variation for a discrete time series $X(t_1), X(t_2), \ldots, X(t_N)$ is a simple extension of the quadratic variation $Q(t) = \lim_{n \to \infty} Q_n$ where:

$$Q_n = \sum_{k=0}^{N/n-1} |X_{(k+1)n} - X_{kn}|^2. \tag{2.34}$$

Here the index n serves a similar purpose as the τ in Eq. 2.32 by giving the variation for a certain small 'lag' or delay. If the process $X(t)$ is taken as ordinary 1D Brownian motion then there is a clear connection with the variance of the underlying stochastic input. Indeed, in that case, the quadratic variance is just $\lim_{n \to \infty} \langle Q_n(t) \rangle = 2Dt$. The p-variation replaces the exponent with p:

$$V_n^{(p)} = \sum_{k=0}^{N/n-1} |X_{(k+1)n} - X_{kn}|^p. \tag{2.35}$$

The p-variation has some useful properties [58]. First is that it is easy to compute – Eq. 2.35 is a simple expression. For FBM, $V_n^{(p)}$ transitions from a decreasing function of n to an increasing function of n at the point $p = 1/H$. For FLSM the picture is more complex due to the fat tails. For $H < 1/\alpha$, the picture is the same as FBM, but for subdiffusion, $V_n^{(p)}$ will only decrease with n. A summary of these behaviors is given in the following table. However, a p-variational analysis can be unwieldy to interpret. An application will be shown in the next section.

As a final note of caution, the four processes outlined here only represent the most simplistic and basic models of anomalous diffusion. Even for these few, it is clear that statistical tests are not of sufficient sophistication. The top performers in the AnDi Challenge [50], which tasks entrants with identifying underlying processes and parameters from sample

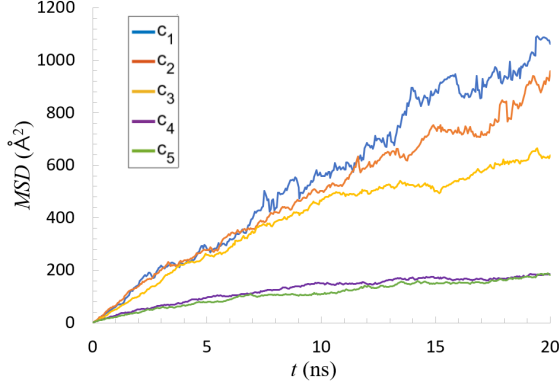| process	$MSD(x)$	$M_N(\tau)$	behavior of p-variation $V_n^{(p)}$ with n
CTRW	$\propto t^{2H}$	$\propto \tau^{2H-1}$	increasing to decreasing at $p = 2$
FBM	$\propto t^{2H}$	$\propto \tau^{2H}$	increasing to decreasing at $p = 1/H$
FLSM ($H < 1/\alpha$)	$\propto t^{2H}$	$\propto \tau^{2H}$	increasing to decreasing at $p = 1/H$
FLSM ($H > 1/\alpha$)	$\propto t^{2H}$	$\propto \tau^{2H}$	decreasing

Table 2.1: Expected results for statistical tests on CTRW, FBM, and FLSM.

trajectories, were the flexible neural network approaches and not strict statistical methods. Furthermore, there are many additional models that are themselves more complex. Ref. [55], for instance, includes 19 different models in their overview. Many of these models try to incorporate spatial or temporal variation by allowing parameters to change in time/space or including confinement or trapping. A typical approach, and one of the tests included in [50], is to segment a time series into separate regions with distinct behavior. Of course, for very noisy processes this approaches a form of art more than science. This is all to say that this field of study is far from mature.

2.3.1 Application of Statistical Tests

In Ref. [59] the aforementioned statistical techniques are applied to a molecular dynamics simulation that exhibits network formation. In that system, various concentrations of mucin are inserted and allowed to diffuse and form both hydrophobic and hydrogen bonds with each other. Increasing the concentration beyond a certain point leads to an onset of crowding and a transition in the behavior of the system. Full details of the simulation are given in Appendix A.

The movements of these mucin molecules and the total number of bonds formed at any given time are stochastic variables that may exhibit anomalous diffusive behaviors, see Fig. 2.7. That particles or polymers within a network experience anomalous diffusion under certain circumstances is already known [60, 61, 62] but whether this is reflected in the interaction dynamics is not well studied.

Figure 2.7: Averaged MSD for atoms within mucin molecules for each simulated concentration and fit values for the diffusion exponent α^* from Eq. 2.36. [59]

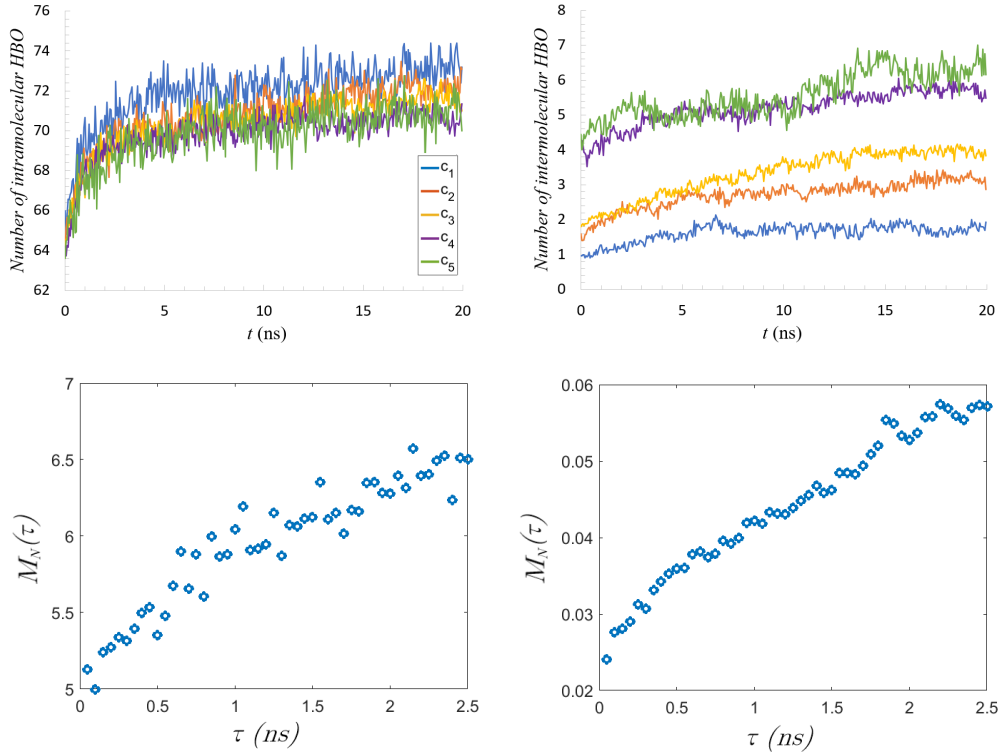| Conc.	α^*	St Dev
c_1	0.931	0.008
c_2	0.826	0.006
c_3	0.662	0.008
c_4	0.517	0.007
c_5	0.610	0.005

Figure 2.8: Top: Averaged number of formed hydrogen bonds for each concentration. Bottom: Sample $M_N(\tau)$ of formed hydrogen bonds for concentration c_1. [59]

The MSD average over all mucin atoms in all simulation runs for each concentration is shown in Fig. 2.7. Each concentration is an increment of 5 mucin molecules. The sublinear behavior is clear and can be fit to the equation for 3D diffusion,

$$MSD(t) = 6Dt^{\alpha*}. \tag{2.36}$$

Here $\alpha^* = 2H$ is referred to as the diffusion exponent. The values for α^* are shown alongside the time series in Fig. 2.7 and range from 0.517 to 0.931. This is subdiffusive and thus it is reasonable to question if one of the processes discussed in the previous section may be the best model. Fig. 2.7 can be combined with an analysis of the time evolution of inter- and intramolecular hydrogen bonds presented in Fig. 2.8. The lower portion shows a representative plot $M_N(\tau)$ for concentration c_1, i.e. the application of Eq. 2.32, for the data above it. The near linearity suggests a CTRW would model the process poorly [63, 55].

A p-variational test can in the subdiffusive case discriminate between the remaining FBM and LSM [58]. For LSM $V_n^{(p)}$ will always be a decreasing function of n. Roughly this is because the size of the largest individual deviations ($|X_{(k+1)n} - X_{kn}|$ in Eq. 2.35) do not meaningfully increase by adding more steps, i.e. increasing n, for Lévy noise due to its heavy tails. This is not the case for FBM, so increasing the importance of large deviations by increasing the exponent p will eventually reverse its trend with n (cf. Eq. 2.35).

Figs. 2.9, 2.10 & 2.11 show the p-variation for concentrations c_1, c_2, and c_4, respectively. It is customary to label values of p as ratios because it is expected to see a change in behavior at $p = 1/H$. This reversal of trend can be seen in the upper plot, representing intermolecular bonds, for each. That this occurs roughly at $p = 1/0.5$ implies a Hurst exponent $H \sim 0.5$, suggesting that this particular variable actually displays normal diffusion.

The plots of intramolecular bonds are less clear. Concentrations c_1 and c_4 showed significant departure from FBM-like behavior. The largest p values have no clear trend and look chaotic and noisy. It is possible that the noise is becoming fat-tailed but there is not

Figure 2.9: p-variation versus n (cf. Eq. 2.35) for intermolecular (top) and intramolecular (bottom) hydrogen bonds for concentration c_1. [59]
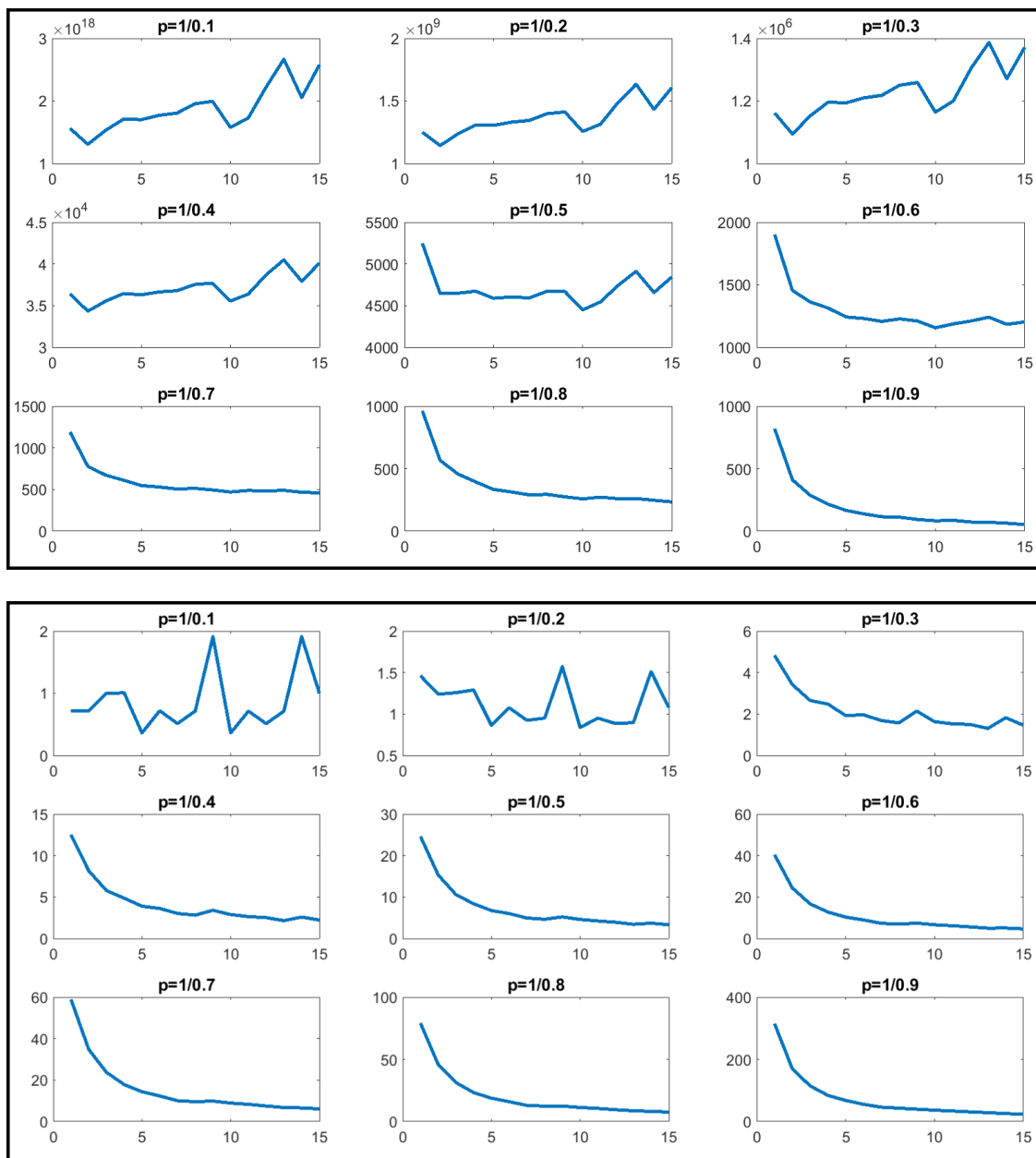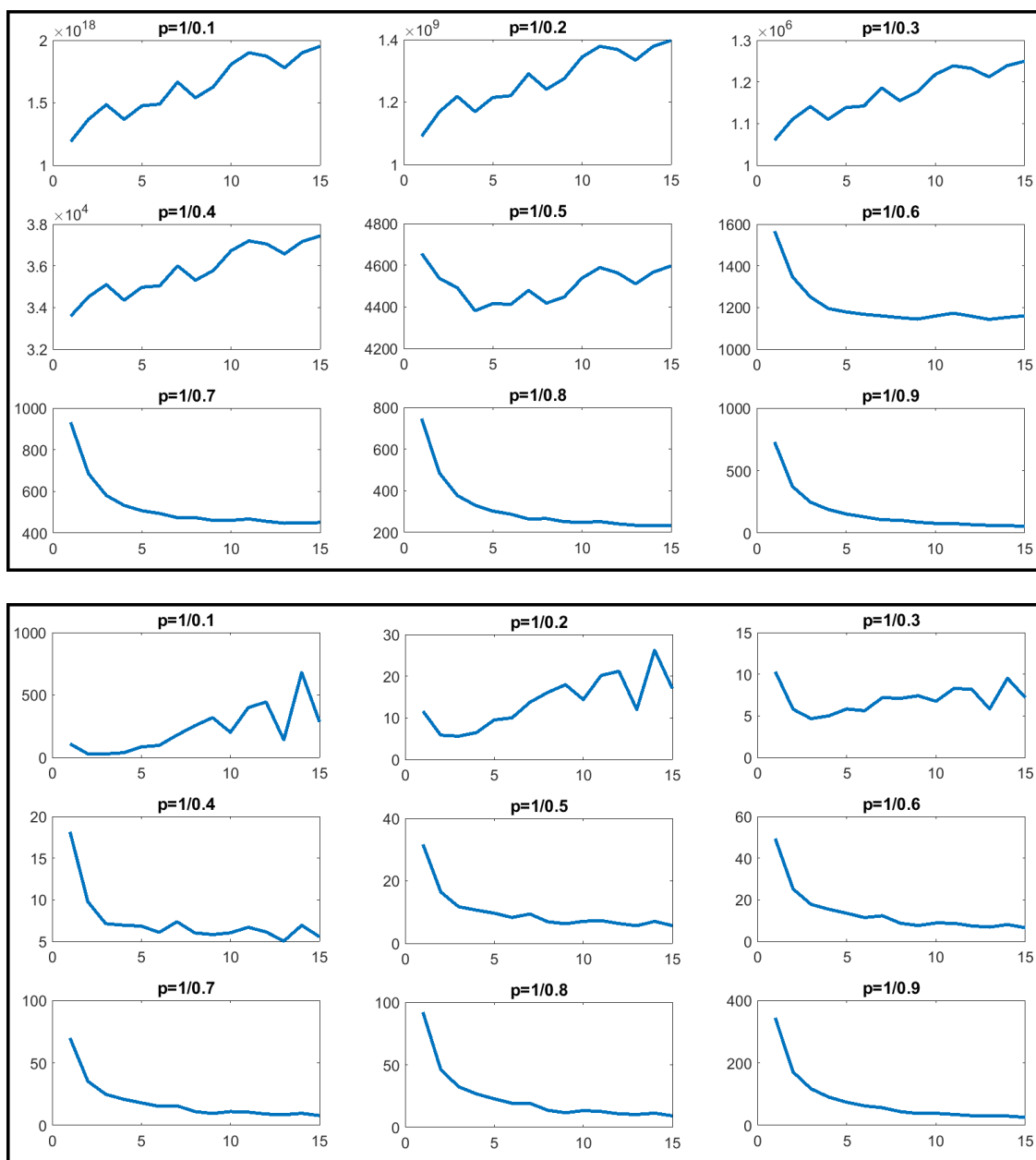
Figure 2.10: p-variation versus n (cf. Eq. 2.35) for intermolecular (top) and intramolecular (bottom) hydrogen bonds for concentration c_2. [59]
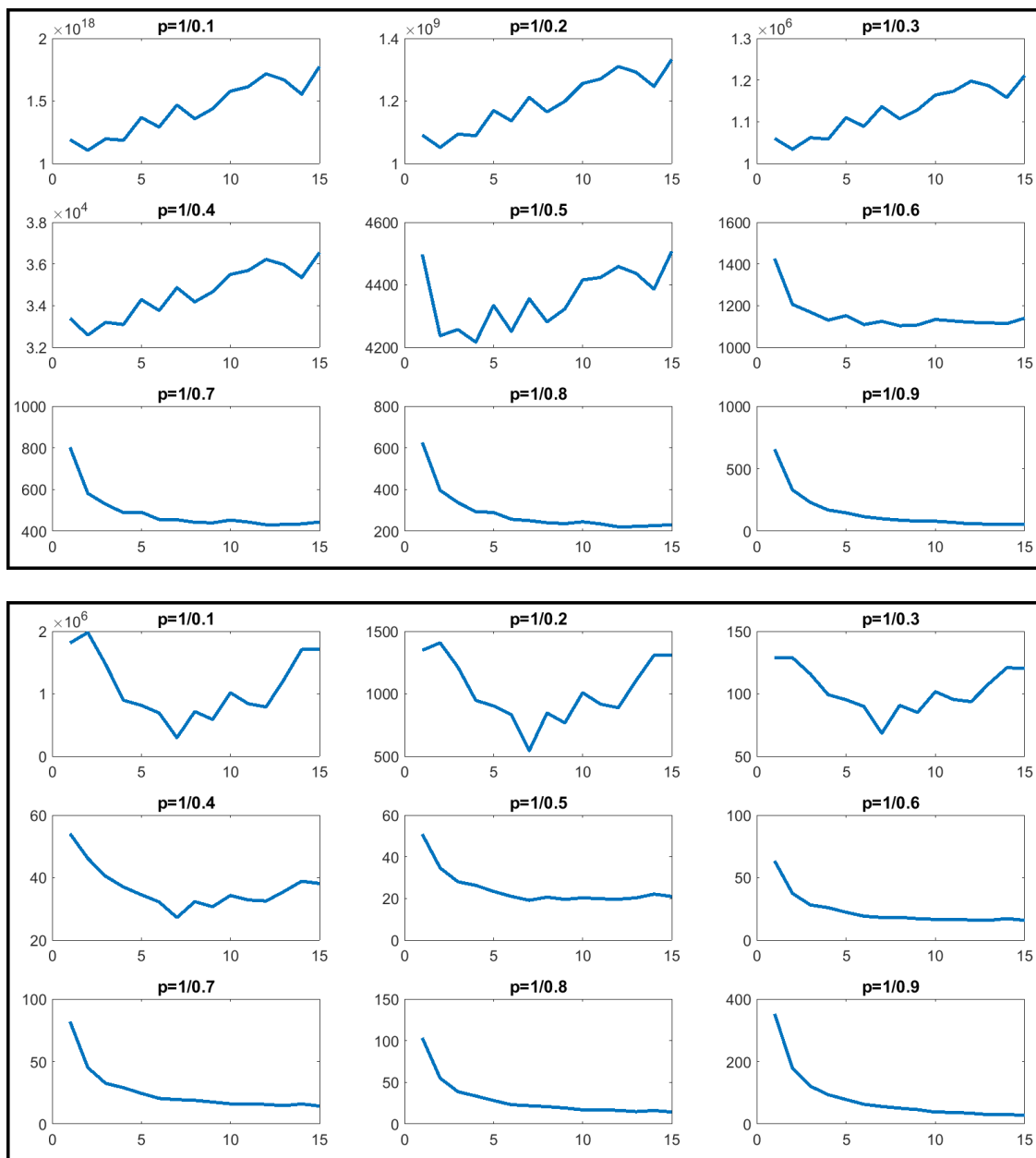
Figure 2.11: p-variation versus n (cf. Eq. 2.35) for intermolecular (top) and intramolecular (bottom) hydrogen bonds for concentration c_4. [59]

sufficient data to be conclusive in that respect. However, even for the other three cases the change in behavior occurs for a value $p > 1/0.5$. This again implies $H < 0.5$ and the presence of a positive correlation in the intramolecular dynamics throughout the simulation. This is sensible as any major changes in the number of intramolecular bonds are likely due to conformational changes induced by interactions with other molecules that resolve over longer periods.

2.4 Application to Harmonic Potential

At the end of Sec. 2.2.1 a Euler discretization of Eq. 2.6 was described which approximates the force on a particle as constant within each timestep. It must be noted that this scheme is not on its own sufficient for an investigation of the asymmetry presented in Fig. 2.5 in which the forward-time direction can be discerned. The linear approximation of the potential produces in our case:

$$\Delta x_i = -A x_i \Delta t + \theta_{i,\alpha} \Delta t^{1/\alpha}, \tag{2.37}$$

where $\theta_{i,\alpha}$ is the i-th random number drawn from a distribution with $\sigma = 1$. The $\Delta t^{1/\alpha}$ emerges from the necessity of scaling; the effect of many small timesteps must accumulate to that of a singe large timestep of equivalent duration; a property known as 'stability under addition' [39]. For normal diffusion where $\alpha = 2$ the exponential tail of the Gaussian term practically guarantees the linear approximation is sufficient. A small timestep ensures the particle never receives a kick that is large enough to move it over a distance where the curvature of the potential may be nonnegligible. Such is not the case for Lévy noise. Consider again one of the large jumps from Fig. 2.5. Under a Euler scheme the particle, which begins its jump near the bottom of the well, would experience almost no force from the potential during its climb - despite the force being so significant that the particle would make almost the entire return trip in the subsequent step.

Because of the scaling behavior implied by power law tails this cannot be overcome by

taking a small enough Δt. From Eq. 2.8, the tail behavior follows $p_\alpha(z) \propto \frac{\sigma^\alpha}{|z|^{\alpha+1}}$. Again, maintaining the scaling in time requires $\sigma^\alpha = (\Delta t^{1/\alpha})^\alpha = \Delta t$, so taking a timestep that is a factor λ smaller leads to kicks of a size larger than $z = z^\star$ to be a factor λ^{-1} times rarer. However, since the simulation now contains λ times as many intervals, the total number of large kicks remains the same.

For the parabolic potential of Fig. 2.5, there is a straightforward solution to this large-kick problem. Within a single timestep from x_i to x_{i+1}, the kick $\xi_\alpha(t_i) = K$ is constant and Eq. 2.6 describes an exponential relaxation to the point $x = K/A$ for a duration Δt. In other words, we can take the solution:

$$x_{i+1} = (x_i - K/A)e^{-A\Delta t} + K/A, \tag{2.38}$$

as the new position without the need for further approximation. It is readily verified that for sufficiently small Δt and K, the above equation readily reduces to the Eulerian $\Delta x_i \approx (-Ax_i + K)\Delta t$.

2.4.1 The Position Distribution in a Harmonic Potential

Alpha-stable noise can be readily generated for a given α parameter from functions already available in, for instance, *Mathematica*. To quantify the breaking of microscopic reversibility, we categorize steps of a time series into 'climbing' and 'descending'. A step from j to $j+1$ is defined as climbing if $|x_{j+1}| > |x_j|$ and descending if $|x_{j+1}| < |x_j|$. Let N_f be the number of climbing steps when viewing the time series forward in time and N_b be the number of climbing steps when the the time series is read backwards. Notice that N_b simply represents the number of descending steps in the original time series. With that in mind, we adopt

$$r = \frac{N_b - N_f}{N_b + N_f} \tag{2.39}$$

as a measure of the time reversal asymmetry. This metric ranges from $r = 0$ for an equal number of climbing/descending steps to $r = \mp1$ for a series that is all climbing (-1) or descending $(+1)$ steps. Again, a difference from $r = 0$ implies a breaking of microscopic reversibility, nonequilibrium, and the further consequences that entails.

Because we are dealing with a stochastic process, we expect r in our case to differ from zero even when microscopic reversibility holds. For N steps, $\frac{1}{2}N$ are expected to be climbing, with a standard deviation of $\sqrt{\frac{1}{2}N}$. From this we infer that, for the case of time-reversal symmetry, the value of r comes with a coefficient of variation (the ratio of standard deviation and average) of $1/\sqrt{N}$. Only if $|r|$ comes out significantly larger than $1/\sqrt{N}$ can we conclude that time-reversal symmetry is violated. In the general case of the harmonic potential, we expect r to be positive for Lévy noise.

As the system moves away from equilibrium (by decreasing α from 2 to 0), the r value moves slowly away from $r = 0$, but this is not the only dependence. Fig. 2.12 shows the results from many stochastic simulations of a Lévy noise driven particle in a harmonic potential. Each curve represents a different value of $\Delta t \times A$. Recalling that Eq. 2.38 describes a simple exponential relaxation, A can be identified with the relaxation time, e.g. $A = 1/\tau$. The product with Δt is then a dimensionless ratio that specifies in a relative sense how much relaxation takes place between timesteps. In alternative language, decreasing Δt can be thought of as increasing the sampling rate for measurement on a system with an inherent characteristic timescale $\tau = 1/A$.

It is intuitive that sampling too slowly, corresponding to a $\Delta t \times A \gtrsim 1$, leads to the appearance of microscopic reversibility. In these cases, the particle always has the time to relax to the point $x = -K/A$, where the force from the potential equals the force from the random kick. Any memory is 'destroyed' and we are just left with the (scaled) kick distribution itself.

For $\Delta t \times A \to 0$, the r value as a function of α approaches a step function centered at $\alpha = 1$. The particle spends an infinite number of timesteps relaxing after a large jump. Since
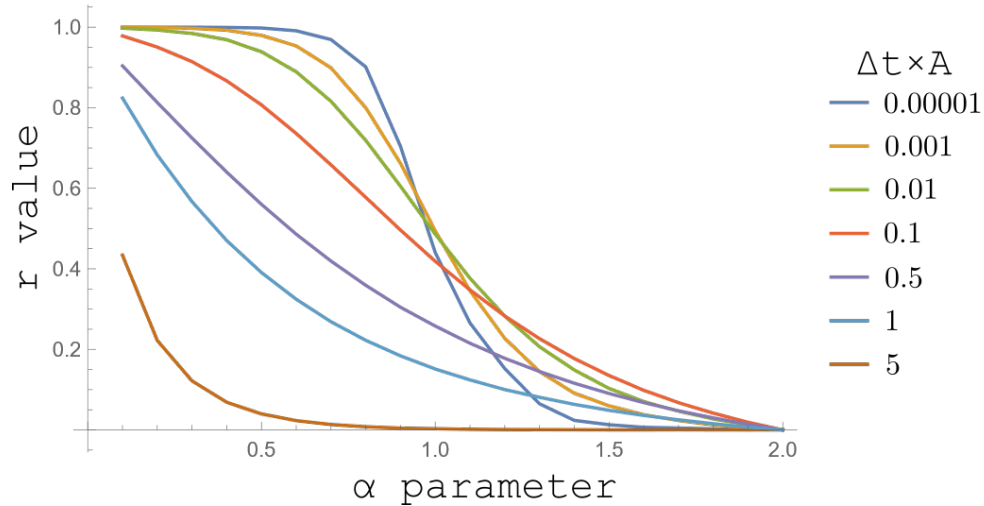
Figure 2.12: The time-reversal asymmetry parameter, r, vs the stability index, α, that characterizes the noise. The curves result from stochastic simulations for different values of Δt and taking $A = 1$. [1]

the position distribution does not scale with Δt, what ultimately determines the value of r is how the position distribution compares with the scaled kicksize distribution. For $\alpha < 1$, reducing Δt rapidly shrinks the stochastic contribution in comparison to the linear force term. This is apparent from the scaling factor $\Delta t^{1/\alpha}$ on the noise term in Eq. 2.37. A large jump causes a downslide of infinitely many steps, leading to $r \to 1$. For $\alpha > 1$, the scale factor $\Delta t^{1/\alpha}$ is instead sublinear. The noise contribution thus shrinks more slowly than the drift term as Δt decreases. The potential induced drift which may be apparent over longer periods is overwhelmed timestep to timestep, leading to $r \to 0$.

The curves in Fig. 2.12 are from stochastic simulations, but can also be obtained from numeric integrations involving the kick and position distributions. The kick distribution was the input to Eq. 2.6 and is thus known, but the position distribution must be derived. It should also be pointed out that the position distributions deriving from Fig. 2.5b and Fig. 2.5c are different. A Boltzmann distribution will result from Fig. 2.5b, but this is no longer the rule with $\alpha < 2$. Luckily there is another tool to bring to bear. In the first decade of the last century Einstein and Smoluchowski separately showed that diffusion and Brownian motion are connected at the microscopic level by retrieving the diffusion coefficient

$D = \langle x^2 \rangle / 2t$ from the assumptions of Brownian motion [64, 65, 66]. Practically this provided the relation between the speed of diffusion and the temperature dependent size of Brownian 'kicks', but more importantly it paved the way for the use of probability density functions to describe the time evolution of stochastic processes – with the Fokker-Planck equation as the archetypal example.

The equivalent Fokker-Planck equation for Gaussian noise is well known [67]. For the stochastic Langevin (eq 2.6) the equivalent Fractional Fokker-Planck equation is [44]:

$$\frac{\partial P(x,t)}{\partial t} = A \frac{\partial [x P(x,t)]}{\partial x} + \sigma^\alpha \frac{\partial^\alpha P(x,t)}{\partial |x|^\alpha}, \tag{2.40}$$

The fractional derivatives will be dealt with by their Fourier space representations where derivate-taking becomes multiplicative: $\frac{\partial^\alpha}{\partial |x|^\alpha} f(x) = \int_{-\infty}^{\infty} \frac{dk}{2\pi} e^{-ikx} |k|^\alpha \tilde{f}(k)$ with $\tilde{f}(k)$ as the Fourier Transform of $f(x)$. This provides a straightforward method for retrieving the eventual stationary state analogous to the Boltzmann distribution - set the left hand side to zero, transform to Fourier space, and solve the resultant differential equation:

$$-Ak \frac{d\tilde{P}_{st}(k)}{dk} - \sigma^\alpha |k|^\alpha \tilde{P}_{st}(k) = 0. \tag{2.41}$$

Yielding the solution:

$$\tilde{P}_{st}(k) = \exp\left[-\frac{\sigma^\alpha |k|^\alpha}{A\alpha}\right]. \tag{2.42}$$

This solution can be identified with the noise distribution which generated it, Eq. 2.7 (for $\mu = 0$). Both are Lévy distributions with the same α, but the original σ scale parameter is now $\sigma' = \sigma/(A\alpha)^{1/\alpha}$. If we scale the system by taking $A = 1$ and $\sigma = 1$, we have

$$\tilde{p}(k) = \exp[-|k|^\alpha] \tag{2.43}$$

for the kicksize distribution and

$$\tilde{P}_{st}(k) = \exp[-|k|^\alpha/\alpha] \qquad (2.44)$$

for the position distribution. This probability distribution may not have a nice analytic expression in real space, but because the $1/\alpha$ in the exponent translates to a scale factor it can be written as a scaled version of the kicksize distribution $p(x)$. Taking that scale factor as σ' leads to

$$P_{st}(x) = \frac{1}{\sigma'} p\left(\frac{x}{\sigma'}\right), \qquad (2.45)$$

for the probability.

2.4.2 Asymmetry Parameter for the Parabolic Well

Let $P_{climb}(x)$ be the probability that, for a particle at position x, the next step brings the particle to a higher position in the parabola. For the fraction of steps that are climbing steps, φ_{climb}, we then have

$$\varphi_{climb} = \int_{-\infty}^{\infty} P_{climb}(x) P_{st}(x) \, dx, \qquad (2.46)$$

where $P_{st}(x)$ is the stationary probability-density distribution for which $\tilde{P}_{st}(k)$, cf. Eq. (2.4.1), is the generating function. The parameter r (cf. Eq. 2.39) is related to φ_{climb} through

$$r = 1 - 2\varphi_{climb}. \qquad (2.47)$$

The argument presented in the previous section makes clear that, for $0 < \alpha < 2$, we should have $0 < \varphi_{climb} < 1/2$ and, consequently, $0 < r < 1$.

For positive x_i, the probability $P_{climb}(x_i)$ can be split out as follows: $P_{climb}(x_i) = P(x_{i+1} > x_i) + P(x_{i+1} < -x_i)$. With the (scaled) Eq. (2.38) this means that the kicksize, K, has to

follow either $K > x_i$, or $K < -sx_i$, where

$$s = \frac{e^{\Delta t} + 1}{e^{\Delta t} - 1}. \tag{2.48}$$

Generalizing to any real x, it is thus found that

$$\varphi_{climb} = \int_{-\infty}^{\infty} \left[\int_{-\infty}^{-sx} p(\xi)\,d\xi + \int_{x}^{\infty} p(\xi)\,d\xi \right] P_{st}(x)\,dx. \tag{2.49}$$

The inner integrals can be replaced by their respective cumulative distribution functions (cdf) (which are available in *Mathematica*). The symmetry in x, furthermore, allows us to integrate over half the domain and double the result:

$$\varphi_{climb} = 2 \int_{-\infty}^{0} \left[\mathrm{cdf}(sx) + \mathrm{cdf}(x) \right] P_{st}(x)\,dx. \tag{2.50}$$

This integral reproduces the curves of Fig. 2.12 but does not offer much intuition on why there is a transition at $\alpha = 1$. This can be made clear through an analysis of some special cases.

The $\alpha = 2$ case. - For $\alpha = 2$, the statistics are not "polluted" by Lévy jumps. We take Δt to be sufficiently small for the Euler scheme approximation to Eq. (2.6) to apply. The piecewise-linear solution that the Euler scheme gives will be more accurate as Δt is taken smaller. For the increments we have

$$\Delta x_i = -x_i \Delta t + \theta_{\alpha=2,i}\sqrt{\Delta t}, \tag{2.51}$$

where $\theta_{\alpha=2,i}$ is the i-th random number drawn from a distribution with $\sigma = 1$. From Eq. (2.51) it is obvious that, for one particular timestep, the deterministic part of the motion becomes negligible if $\Delta t \to 0$. In that case $(\Delta x)^2$ and Δt are of the same order, i.e., $(\Delta x)^2 \sim \Delta t$. We take two nearby points, x and $x + \Delta x$, where $x > 0$ and $\Delta x > 0$. We

next focus on the particles that move between these points in *exactly* Δt. If microscopic reversibility applies, then the traffic in both directions should be equal. From Eq. (2.51) we find that in order to move from x to $x + \Delta x$ in time Δt, a kick $\theta_{\alpha=2,i} = x\sqrt{\Delta t} + \Delta x/\sqrt{\Delta t}$ is required. In order to move from $x + \Delta x$ to x in Δt, we need $\theta_{\alpha=2,i} = (x + \Delta x)\sqrt{\Delta t} - \Delta x/\sqrt{\Delta t}$. Taking into account the different probability densities, P_{st}, at x and $x + \Delta x$, we find for the difference, $\hat{r}$, between descending and ascending traffic:

$$\hat{r} = P_{st}\left(x + \Delta x\right) p\left((x + \Delta x)\sqrt{\Delta t} - \Delta x/\sqrt{\Delta t}\right) -$$
$$P_{st}(x) p(x\sqrt{\Delta t} + \Delta x/\sqrt{\Delta t}). \tag{2.52}$$

Note that $\hat{r}$ is different from r (cf. Eq. (2.39)) in that it is local and has a dimension of square density. Next substituting $P_{st}(x) = 1/\sqrt{2\pi}\exp\left[-x^2/2\right]$ and $p(x) = 1/(2\sqrt{\pi})\exp\left[-x^2/4\right]$ for the position distribution and the kicksize distribution respectively, we infer after some algebra:

$$\hat{r} \propto \exp\left[-\frac{1}{2}x^2 - \frac{1}{4}\frac{(\Delta x)^2}{\Delta t} - \frac{1}{2}x(\Delta x) - \frac{1}{4}x^2(\Delta t)\right] \times$$
$$\left(\exp\left[-\frac{1}{4}(\Delta x)(\Delta t)(2x + \Delta x)\right] - 1\right). \tag{2.53}$$

For $(\Delta x)^2 \sim \Delta t$, only the first two terms in the exponent in the prefactor are finite. The second exponential term, the one in the round brackets, has terms in the exponent that can all be made arbitrarily small by picking Δx and Δt sufficiently small. We thus find that $\hat{r}$ approaches zero as $\Delta t \to 0$ and $\Delta x \to 0$. Every trajectory between any two points (t_1, x_1) and (t_2, x_2) can be constructed from small linear steps that each have $\hat{r} \to 0$. It can be concluded that microscopic reversibility applies for Gaussian noise. We thus also have $r = 0$ (cf. Eq. (2.39)) for $\alpha = 2$.

The $\alpha = 1$ case. Only for $\alpha = 1$ are the kicksize distribution, cf. Eq. (2.43), and the position distribution, cf. Eq. (2.44), identical. For this case it is easily proven that $r = 1/2$ if

$\Delta t \to 0$. Taking $f(x) = \int_{\xi=x}^{\infty} p(\xi)\,d\xi$ and next realizing that $f(0) = 1/2$ and $f(x \to \infty) = 0$, we see how the integral Eq. (2.49) reduces:

$$
\begin{aligned}
\varphi_{climb} &= 2\int_{x=0}^{\infty} \left(\int_{\xi=x}^{\infty} p(\xi)\,d\xi \right) p(x)\,dx \\
&= 2\int_{x=0}^{\infty} \left(\int_{\xi=x}^{\infty} p(\xi)\,d\xi \right) \left(-\frac{d}{dx} \int_{\xi=x}^{\infty} p(\xi)\,d\xi \right) dx \\
&= -2\int_{x=0}^{\infty} f(x) f'(x)\,dx = -f^2(x)|_{x=0}^{\infty} = \frac{1}{4}.
\end{aligned}
\tag{2.54}
$$

With Eq. (2.47), this result leads to $r = 1/2$.

Through Eqs. (2.49) and (2.50) it is even possible to obtain an analytic result for $\varphi_{climb}^{\alpha=1}$ for a finite Δt. The *Mathematica* package readily gives the analytic result:

$$
\varphi_{climb}^{\alpha=1} = \frac{1}{8} + \frac{\Phi\left(\frac{1}{s^2}, 2, \frac{1}{2}\right)}{4\pi^2 s} + \frac{\log(s)\coth^{-1}(s)}{\pi^2},
\tag{2.55}
$$

where $\Phi(.,.,.)$ represents the so-called Lerch Transcendent, i.e. $\Phi(z, s, \beta) = \Sigma_{n=0}^{\infty} z^n/(n+\beta)^s$. In agreement with what Fig. 2 shows, this analytic result has r going down from $r = 1/2$ to $r = 0$ as Δt gets larger.

The $\alpha \to 0$ case.

For $\alpha = 0$ the generating function is a constant and this implies that the probability distribution is a dirac delta function. In the $\alpha \to 0$ limit the probability distribution looks like a sharp spike at $x = 0$ with power law tails. From Fig. 2 it appears that the climbing fraction φ_{climb} approaches zero in the $\alpha \to 0$ limit. Going back to Eqs. (2.44) and (2.45), we see that the α in the denominator of the exponent in $\tilde{P}_{st}(k)$(cf. Eq. (2.44)) translates into a scaling factor $\sigma' = (1/\alpha)^{1/\alpha}$ for $P_{st}(x)$. This means that for $\alpha \to 0$, the position distribution $P_{st}(x)$ is wider than the kicksize distribution $p(\xi)$ by a very large factor. How this leads to $\varphi_{climb} \to 0$ can be understood from a Langevin perspective by realizing that after a large Lévy jump that drives the particle high up the parabola, it will, at $\Delta t \to 0$, take an infinite number

of timesteps to slide down again. In the context of Eqs. (2.49) and (2.50), the $\varphi_{climb} \to 0$ result can be understood after realizing that cdf(x) decreases from 0.5 to 0 as x increases from $x = 0$. If $P_{st}(x)$ is much wider than $p(\xi)$, then cdf(x) will be effectively zero for most of the relevant domain of $P_{st}(x)$ and $\varphi_{climb} = 0$ will result.

Most natural signals appear to be not too far from equilibrium; Mandelbrot's famous cotton stocks and Peng's study of heart interbeat intervals both exhibited $\alpha = 1.7$ [18, 27]. The regime of interest is then just below $\alpha = 2$. From Fig. 2.12 it can be seen that there is a maximization of symmetry breaking in the $1 < \alpha < 2$ interval for $\Delta t \times A \approx 0.1$. Sampling at approximately ten times the characteristic timescale of the system apparently optimizes the trade-off between increasing the number of steps on a downslide and 'losing' individual downward steps to noise.

A noisy downslide is still a downslide – the r enhancement via what is essentially averaging is purely due to the chosen construction of Eq. 2.39, which discards information about the distances traveled for simplicity. This feature is ultimately what allows us to create a unique equivalence between calculated r-values in a sample time series and the underlying α parameter. Fig. 2.13 shows the behavior of this maximized r near $\alpha = 2$, and was calculated by numerically integrating the probability to see a climbing step over the entire position distribution for a variety of α and Δt values.

2.4.3 Asymmetry Analysis of Solar Flare Data

We propose that establishing the value of r from the observed data and next using the patterns observed in Figs. 2.12 & 2.13 to determine the value of α is in many cases a simple, robust, and effective method. Our method is suitable in case of a data stream as in Fig. 2.5c, i.e. a data stream that exhibits occasional large jumps. These jumps are to have power-law-distributed magnitudes and are to be followed by a slower relaxation back to the baseline. This is indicative of Lévy noise in a parabola (cf. Fig. 2.5a) being the appropriate model. As was pointed out before, with a parabolic potential the α that characterizes the
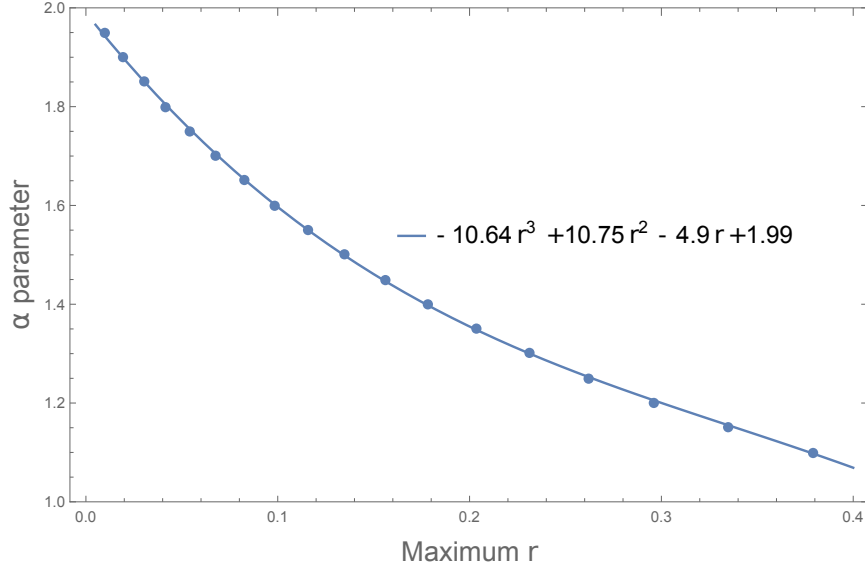
Figure 2.13: Numerically calculated relation between the maximum r-value obtained by undersampling and the underlying α parameter. The equation is a cubic best fit. [1]

position distribution $P_{st}(x)$ is the same as the α that characterizes the noise term $\xi_\alpha(t)$. In determining the value of r, we are taking differences between subsequent numbers in a time sequence. So in our method the order of the sampled data points is essential.

In Fig. 2.5b and 2.5c it is the value of x that constitutes the signal that is followed over time. It should be noticed that if the value of x^2 is followed instead, climbing steps remain climbing steps and non-climbing steps remain non-climbing steps, i.e. the value of r is not affected. As a matter of fact, for any odd or even $f(x)$ where $f(x)$ is increasing for $x > 0$, the same value for r ensues.

With a simulation as in Fig. 2.5 it is unambiguous whether a step is a climbing step or not. After all, we know that $x = 0$ represents the bottom of the parabolic potential. In a real-life sequence of noisy data, however, it may be difficult to establish the precise location of the point x_* where the potential has its minimum. The particle spends the vast majority of its time near the bottom of the parabola and a small variation in the estimate of the $x = x_*$ point, i.e. moving the horizontal axis in Fig. 2.5b and 2.5c a little up or down, will for many steps affect the assessment whether the step is "climbing" or not. Taking the average value of the data sequence as the $x = x_*$ point is not a solution even if the number of data
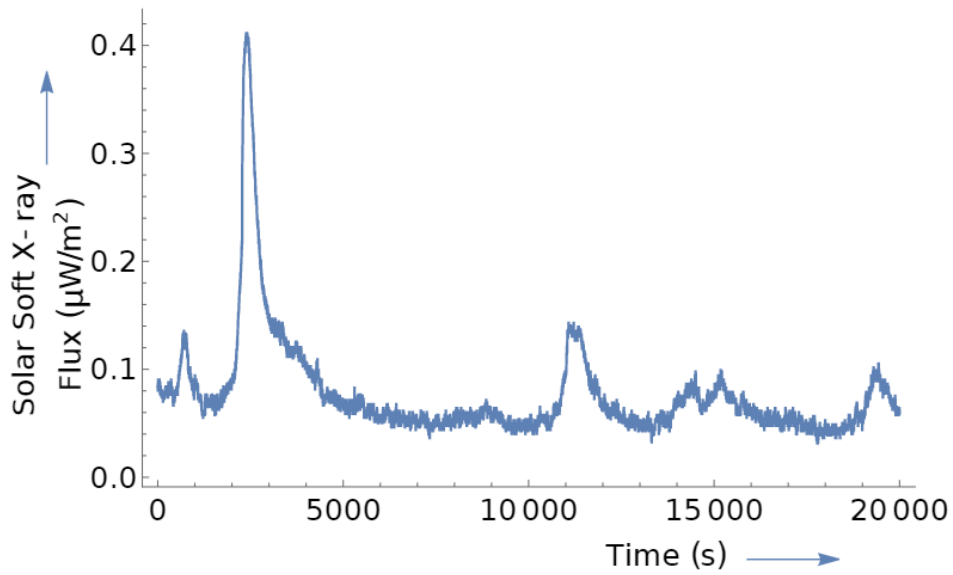
Figure 2.14: An approximately six hour record of solar X-ray fluxes sampled at 2-second intervals. Data was recorded by the *Geostationary Operational Environmental Satellite* (GOES) series and are published online (https://www.ngdc.noaa.gov/stp/satellite/goes-r.html). X-rays were recorded in a window between 1 and 8 Å, the so-called "soft" regime. [1]

points is very large. This is because the average converges slowly or not at all if data have an α-stable distribution. An additional problem occurs when there is a tiny shift in the value of x_* in the course of the data collection.

No vagueness in the estimate of x_*, however, occurs when working with a data stream that can be identified with values that are proportional to $z = (x - x_*)^2 + Z_0$, where Z_0 is a constant. In that case the lowest value of the signal in the entire sequence can be safely taken as representing the bottom of the parabola. Any increase of the signal value from one sample point to the next can then be unambiguously counted as a climbing step. Obviously this applies for any $z = f(x - x_*) + Z_0$ where f is a function that monotonically increases on $(x - x_*) > 0$ and monotonically decreases on $(x - x_*) < 0$. As a first example to illustrate this, think of a room with a thermostat. If the room gets too hot, an air conditioner is turned on. If the room gets too cold, a heater is turned on. The power consumption, as given by the electric meter, will always be positive. As a second example, think of an airplane with mass m for which gravity and the lift force are in balance when the plane flies at an altitude h_0 at a horizontal velocity v_0. There is a restoring force towards h_0; if the plane increases (decreases) altitude, the decreased (increased) air density will decrease (increase) the lift force. Let Δv be the vertical velocity due to the altitude fluctuations and the restoring force. The kinetic energy of the plane relative to a point on the ground is $E_{kin} = \frac{1}{2}m(v_0^2 + \Delta v^2)$ and has the form presented in the first sentence of this paragraph.

Figure 2.14 shows six hours of solar soft X-ray flux as captured by satellite. X-ray fluxes are central in the study of solar flares [68]. A record of solar soft X-ray fluxes going back many years is publicly available through the website of the National Oceanic and Atmospheric Administration. Outliers and a characteristic "shooting up and sliding down" are evident in Fig. 2.14. It is also clear that the sampling rate is fast compared to the rate of relaxation, as the relaxation after a spike lasts a few thousand seconds. This allows for an analysis related to Fig. 2.12.

The differential rotation of the Sun and the convective flows in the Sun's interior stretch
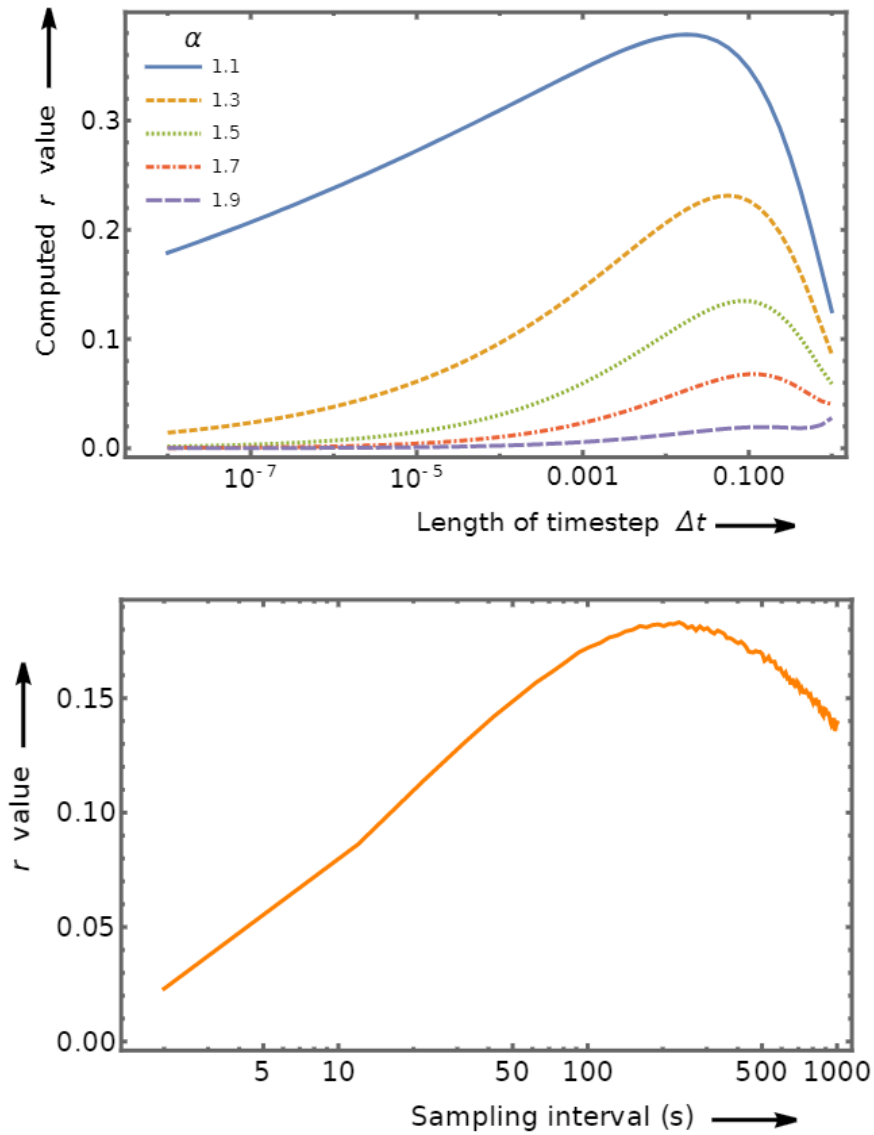
Figure 2.15: The values of r calculated by undersampling. The top figure (a) shows theoretical results following Eqs. (2.46-2.50) for different values of α with $1 < \alpha < 2$. The bottom figure (b) derives from solar soft X-ray data as shown in Fig. 2.14 and computed in intervals of 10 s. [1]

and wrap the magnetic field lines. As the solar cycle progresses the field-line pattern gets more twisted. Solar flares occur as a result of magnetic reconnections, i.e. the field reconfiguring itself and transitioning to a lower energy structure [69, 70]. The peaks in Fig. 2.14 can be associated with solar flares. The distributions of observable quantities that are connected to solar flares have been found to follow power laws [71].

A solar flare's X-rays are in fact bremsstrahlung and thermal radiation (at $> 10^6$ K). These are emitted directly following the explosive release of the reconnection energy. As the energy disperses and dissipates there is ultimately a return to the nonequilibrium steady-state. Figure 2.14 shows the watts per square meter that the detector receives. It is not unreasonable to identify the jump and subsequent relaxation in Fig. 2.14 with a Lévy jump and a subsequent decrease of $V(x)$ in Fig. 2.5a. In other words, we take $\sqrt{\text{power}}$ as the x variable in our analysis. But, as was mentioned before, the same value for r is obtained for any signal that is proportional to z where $z = f(x) + Z_0$ with $f'(x) > 0$ on $x > 0$ and $f'(x) < 0$ on $x < 0$. What matters is that the underlying process giving rise to the movement of x is the noisy particle in the parabolic potential, i.e. Eq. (2.6) and Fig. 2.5a.

The relaxations that are apparent in Fig. 2.14 indicate that Eq. (2.6) and Fig. 2.5a are the right model. The power laws associated with solar flare occurrence tell us that we have Lévy jumps, i.e. $\alpha < 2$.

In Fig. 2.12 it is apparent that for $\alpha > 1$ the value of r does not change monotonically with the timestep length Δt. There appears to be a peak for $\Delta t \approx 0.1$. Here we further explore this feature to establish α for solar soft X-ray fluxes. Figure 2.15a derives from the theoretical analysis using Eqs. 2.46-2.50 and shows r as a function of Δt for different values of α. The apparent maximum can be intuited as follows. To the right of the maximum the number of timesteps in a relaxation back to the baseline after a peak, i.e. the number of descending steps, decreases as Δt is made larger. To the left r decreases because the shrinking timesteps put emphasis on the stochastic ($r = 0$) contribution. The solar flare time series can be viewed as a relaxation process (drift) being driven and obscured by a

noise process (diffusion) with measurements occuring every Δt. The contributions due to drift and diffusion are

$$\Delta x_{drift} \propto \Delta t \ \ \text{and} \ \ \Delta x_{diff} \propto \Delta t^{1/\alpha}, \tag{2.56}$$

respectively. With $1 < \alpha < 2$ it is obvious that for an individual step the diffusive contribution takes on a greater significance if Δt is brought closer to zero. So for $\Delta t \to 0$ diffusion overwhelms drift and the probabilities to be climbing and descending both approach $1/2$. A complete relaxation from a peak back to the baseline will contain more descending steps than climbing steps, but for decreasing Δt that difference will be an ever smaller fraction of the total number of steps involved in the relaxation. As a consequence Eq. (2.39) will yield a smaller value for r. It should also be realized that information about step length is erased when merely counting ascending and descending steps. When relaxing back from a peak to the baseline, the required net descent also occurs when descending and climbing steps are equal in number, but with descending steps being on average longer than climbing steps. Finally, we mention that the above Eq. (2.56) also explains why the method described in this section no longer applies if $\alpha < 1$ – the diffusive component which dominates for small Δt only increases in importance as Δt grows and there is never a maximum.

The α parameter for solar soft X-ray fluxes has also been estimated through scaling properties associated with the power-law tails for $\alpha < 2$ [72]. A block of data that is twice as long will on average yield a maximum data value that is a factor $2^{1/\alpha}$ larger [73]. The slope in a log-log plot of the average maximum value against the block size, next gives the value of $1/\alpha$. We took the data for the years 2011-2016. These years represent a solar maximum during which the flare activity appears fairly constant [72]. Because lengths of data blocks must be powers of two, we ended up cutting off seven months at each end. Using the method of Ref. [72] we thus reproduced the $\alpha = 1.22$ that was also in [72] for prior solar cycles.

Figure 2.15b shows results from measurements of solar soft X-rays. The figure derives again from the 2011-2016 solar maximum with seven months cut off at each end. The shape is visually congruent to shapes seen in Fig. 2.15a. The location of the maximum also

corresponds well - it occurs at a timescale close to a tenth of the observable relaxation time after a peak (cf. Fig. 2.14). An interpolation of this maximum between the curves of Fig. 2.15a leads to an estimate of $\alpha = 1.38$ for the solar soft X-ray flux. In Appendix B we present a step-by-step algorithm to extract the value of α from a stream of sampled data. Our $\alpha = 1.38$ appeared very robust; the same value was found when shorter slices of data (single years or months) were taken. Other methods appeared less robust in their α-estimate when subsets of the entire record were taken (data not shown).

Applying the aforementioned quantile method (cf. Sec. 2.3) [38] to the 2011-2016 solar maximum with seven months cut off at each end, it is found that $\alpha = 1.26$. Quantile-method-estimates for shorter slices of the data appear quite variable. This is likely a reflection of fact that the quantile method estimates more than just the α; the scale parameter, baseline level, and skew of the distribution are also involved and these may drift over time.

Both our r value method and the power-law-tail method of Ref. [72] are aimed at the value of the stability index α. Nevertheless, a drift in the scale parameter σ affects the ultimate estimate for α. For the power-law-tail method it is obvious from Eq. (2.8) that a change of σ during the data stream will "contaminate" the estimate for α. For our r value method the parameter A that characterizes the parabolic potential (cf. Eq. (2.6)) is ultimately incorporated in the scale parameter for $P_{st}(x)$ (see Section III). But A also gives the relaxation time $t_{rel} = 1/A$. A drift in the relaxation time will shift the maximum in Fig. 2.15b to the left or right and can thus affect the estimate for α.

Finally, it is interesting to note that the power-law-tail method of Ref. [72] derives its estimate from the numerical values of the outlier data. The vast majority of the data is effectively not utilized. The order in which the numbers occur is also not used. Our r method exploits the entire data sequence, but discards exact numerical values and focusses on just the sign of the difference between two subsequent data points.

Chapter 3

'Entropy' and Non-Equilibrium

3.1 Introductory Remarks

The previous chapter focuses on how the violation of some of the assumptions that define equilibrium can lead to identifiable consequences such as broken time reversal symmetry and deviations from the Boltzmann distribution. In doing so, the discussion was largely restricted to the simplest case of a single dimension and the analysis was restricted to a statistical one. This chapter will analyze a higher dimensional system and connect the results to the more general thermodynamic concept of entropy.

Imagine a liquid in which "active" particles are suspended. Such "active" particles can be bacteria that propel themselves, i.e. swim. These can also be particles that are manipulated through fields from the outside. Obviously, energy is pumped into such systems and no First Law or any of the concepts mentioned in the previous paragraph applies. Over the last two decades, setups with active particles have been the subject of much experimental and theoretical research.

There are many different ways to model the movements of active particles. One can, for instance, assume that the particle has the same speed all the time and that the change of the direction of motion follows a diffusion equation [74]. The "Run-and-Tumble" model is a

more discrete version of this and it was inspired by the way that *Escherichia coli* bacteria move [75]. Here the particle or bacteria covers a finite-length, straight segment at a constant speed. After coming to a stop it lingers for a moment. It "tumbles" and then picks a new random direction for the next run. There are also different ways to let the active particle interact with the wall of the reservoir in which it swims.

In the analysis below, we return to the random walk, but in two dimensions: at every timestep a direction is picked randomly and a displacement is drawn from a zero-centered distribution (cf. Fig. 3.1). We let the random walks happen in a confinement. Whenever the particle hits the wall, it comes to a standstill. Subsequently, it only moves away from the wall again if a random displacement makes it move inside the circular confinement.

If displacements are drawn from a zero-average Gaussian distribution, we eventually see a homogeneous distribution of particle positions over the entire domain. But if we, instead, draw distances from an α-stable distribution [76, 77, 25, 78] a nonhomogeneous distribution develops.

The Gaussian distribution has an exponential tail, i.e., $p_2(\xi) \propto \exp\left[-\xi^2/2\sigma^2\right]$ as $\xi \to \pm\infty$. Here σ denotes the standard deviation of the Gaussian. The rapid convergence to zero of the exponential tail means that the probability to make a big jump is very small and effectively negligible. Figure 3.1a shows this clearly.

For an α-stable distribution, the asymptotic behavior is described by a power law:

$$p_\alpha(\xi) \propto |\xi|^{-\alpha-1} \quad \text{as} \quad \xi \to \pm\infty. \tag{3.1}$$

Here α is again the stability index for which we have $0 < \alpha < 2$ and when $\alpha = 2$ it is the Gaussian. The power law converges slower than the exponential. A result of this is that outliers, i.e. large "Lévy jumps," regularly occur (see Fig. 3.1b). Ultimately, the Lévy walk resembles a run-and-tumble walk, but, following Eq. (3.1), the Lévy jumps have no characteristic length and the average length of a Lévy jump actually diverges.
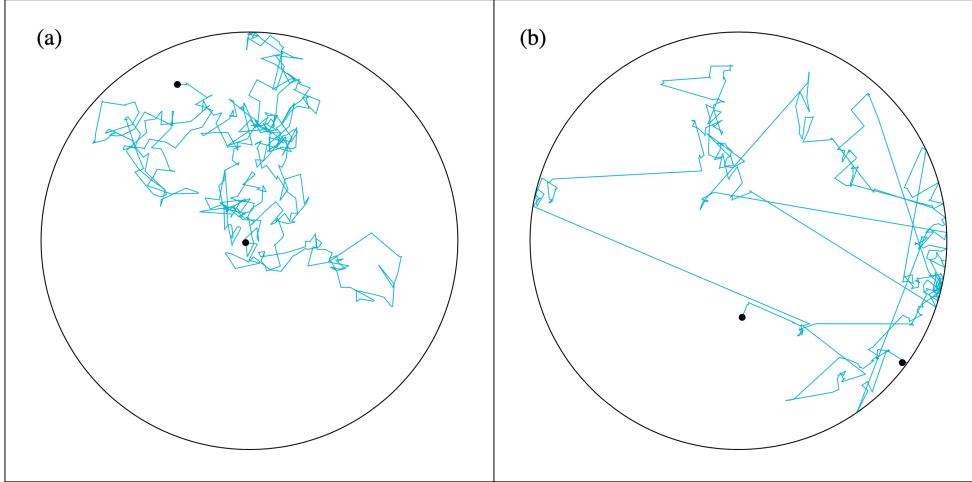
Figure 3.1: Random walk in a circular domain. Whenever the particle hits the wall, it comes to a standstill and later it only moves again when a computed step leads to a movement inside the circle. For every step the direction is picked randomly and the displacement is drawn from a (a) Gaussian distribution or from a (b) Lévy-stable distribution. The circle has a radius of 20. Both distributions are symmetric around zero. The Gaussian distribution has a standard deviation of $\sqrt{2}$. For the Lévy-stable distribution we have $\alpha = 1$ and a scale factor of $\sigma = 1$. [2]

As of yet, there is no complete and general theory to explain how and why α-stable distributions are connected to far-from-equilibrium. For many of the phenomena mentioned before, such as the cotton stocks of Mandelbrot or the sudden bursts of solar irradiance, the origin seems to lie somewhere within the dynamics of the system itself. In this sense the α-stable distributions are like $1/f$-noise [26, 79]. The connection of far-from-equilibrium with α-stable distributions and $1/f$-noise is still for the most part a phenomenological one. Interestingly, power law distributions also appear to be driven by living systems, such as the bacteria just described, the foraging of animals [80, 81] (or even humans [82]), or the variability of heart interbeat intervals [83].

Regardless of the source, as mentioned above, nonequilibrium characteristics do emerge when, instead of Gaussian noise, Lévy noise is added to particle dynamics. Sec. 2.4.2 described how an external potential in conjunction with Lévy noise can induce a breaking of microscopic reversibility. The potential creates a time correlation on the diffusing particle - in effect erasing the 'memory' the particle would have of its prior position in a normal

random walk. Because this happens on a characteristic time scale, it was possible to see the after effects of a large jump, deduce the forward time direction, and even estimate the α parameter. The 2D confined random walk, however, imposes no such time correlation.

For the setup that is depicted in Fig. 3.1b, the violation of time-reversal symmetry is in the interaction of the particle with the wall. Elastic collisions have time-reversal symmetry and had we taken the particle in Fig. 3.1b to collide elastically with the wall, forward and backward trajectories would have been indistinguishable. Lévy jumps are rare, but because of their length, they are likely to end at the wall. Once the particle is located at the wall, the probability that already the first subsequent step is a Lévy jump away from the wall is small. Moreover, only a step that leads to movement inside the reservoir will be processed in the simulation. So the particle can "linger" near the wall after hitting it. In the end it appears as if it is easier to get to the wall than it is to get away from it, i.e., it looks as if there is reduced mobility near the wall. Figure 3.2 shows how this is the case on a 1D interval.

In the previous paragraph we put the finger on something that applies generally for active particles in a confinement. They do not distribute homogeneously, but instead accumulate near a wall. It furthermore appears that the accumulation is stronger if the wall has a stronger inward curvature [84]. Active particles tend to get stuck in nooks and corners of a confinement and even more so if the nooks and corners are tighter. This is the phenomenon that we will elaborate on below.

How Lévy particles distribute on a confined 1D segment (cf. Fig. 3.2) can be described with a Fractional Fokker-Planck Equation [85]. The steady-state solution of that equation is available [86]. We show in Appendix D how this solution readily generalizes to higher dimensional setups. Below we examine how Lévy particles distribute over two connected reservoirs where one reservoir is a scaled down version of the other. We will see a deviation from the homogeneous distribution that is obtained when the noise is Gaussian and when equilibrium theory applies.
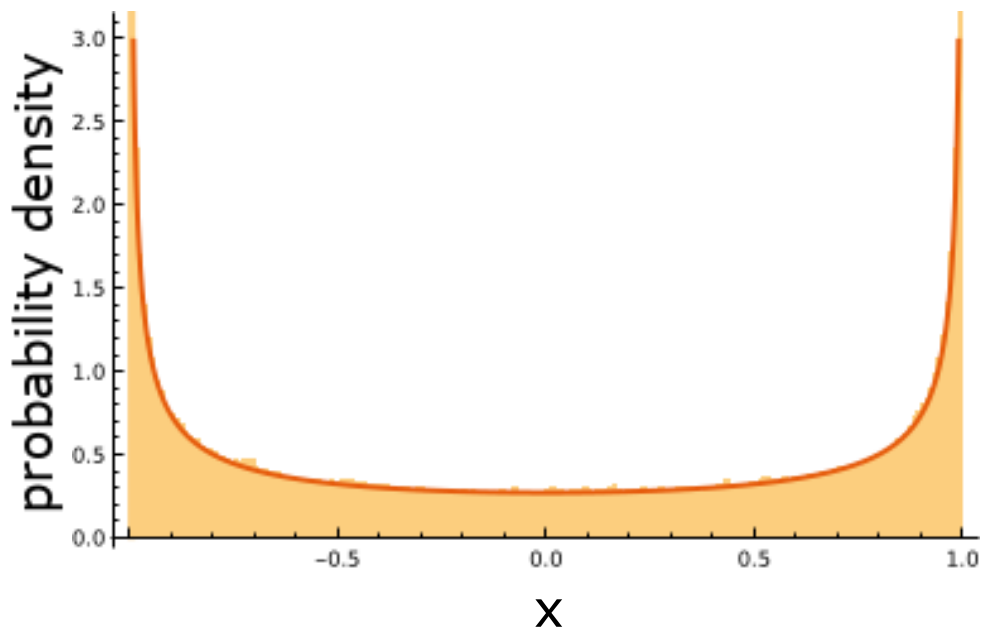
Figure 3.2: A Lévy walk on the interval $-1 \le x \le 1$ (cf. Eq. (3.3)). The value of the stability index is $\alpha = 0.8$. Whenever the particle hits $x = \pm 1$, it stays there until an iteration occurs in the direction away from the wall. The red curve shows the analytic solution (cf. Eq. (3.4)). The normalized histogram is the result of a numerical simulation of Eq. (3.3); the timestep was $\Delta t = 0.001$, there were 10^7 iterations, and the scale factor of the symmetric, zero-centered Lévy distribution was taken to be one. [2]

Suppose we have a volume V with N particles in it. We partition the initially empty V into two reservoirs of a volume $V/2$ each. Next the particles are inserted. Each reservoir has a probability of $1/2$ to receive each particle. Eventually, the probability for all particles to end up in one particular reservoir is 2^{-N}. The probability for an equal distribution over the two reservoirs is $\binom{N}{N/2}2^{-N}$. The binomial coefficient $\binom{N}{N/2}$ grows very rapidly with N.

The reason that the air in a room never spontaneously concentrates in one half of the room is that there is just one way to put all molecules in one chosen half and $\binom{N}{N/2}$ ways to distribute them equally. In other words, the macrostate in which all air is concentrated in one particular half of the room has <u>one microstate</u> and the macrostate with a homogeneous air distribution over the entire room has $\binom{N}{N/2}$ <u>microstates</u>. The entropy, S, of a macrostate can be defined as a scalar value that is proportional to the logarithm of the number of microstates, Ω, of that macrostate, i.e. $S \propto \log \Omega$ [87]. In this case it is obvious that the homogeneous distribution leads to maximal entropy.

With a partition and a pump it is, of course, possible to bring all of the air molecules to one half of the room. Such a process requires energy and with standard thermodynamics the involved energies can be calculated. That energy-consuming, active particles can accumulate in a smaller subvolume does not violate laws of nature, and it is also possible to calculate the entropy change associated with such accumulation. Such calculations are the subject of Sec. 3.4.2.

The ultimate goal would be a Lévy-noise-equivalent of entropy. This would be a quantity that takes its extreme value when Lévy-noise-subjected particles reach a steady state distribution. The Kullback-Leibler divergence [88] is a positive scalar value that can be thought of as a "distance" between two given distributions. The Kullback-Leibler divergence between the steady state distribution and another distribution could be a good candidate. With tools like Noether's Theorem, alternative formulations of active-particle statistical mechanics and of the Fractional Fokker-Planck Equation have been derived [89, 90] and work in this direction appears to be promising.

No general formalism is developed, but we present a setup where the entropy decrease associated with the accumulation can be readily described with simple and intuitive formulae. The nonhomogeneous steady-state distributions that develop in the presence of nonequilibrium noise can be interpreted as dissipative structures [91]. The deviation from homogeneity decreases the entropy. However, active particles pump energy into the system and the dissipative structure ultimately facilitates a steady-state dissipation of energy and production of entropy.

3.2 The 1D and 2D Random Walk in a Confined Domain

We start with the Langevin description of a Brownian walk in 1D:

$$\dot{x}(t) = \sqrt{2D}\,\xi_2(t), \tag{3.2}$$

with diffusion coefficient D and the normally distributed random variable $\xi_2(t)$ as well as that of a Lévy walk in 1D, with the stochastic ordinary-differential-equation and its discretized version, repsectively:

$$\dot{x} = \sigma\,\xi_\alpha(t) \ \ \text{and} \ \ \Delta x_i = \sigma\,\theta_{\alpha,i}\,\Delta t^{1/\alpha}. \tag{3.3}$$

Here the values for θ_α are drawn from a symmetric, zero-centered α-stable distribution with a value of one for its scale factor. The Lévy walk is scale-free, but because $\langle\theta_{\alpha,i}^2\rangle \to \infty$ for $0 < \alpha < 2$, there is no traditional diffusion equation and σ is a mere scale factor.

Figure 3.1 shows simulations of 2D random walks. At every timestep a direction is chosen randomly from a flat distribution between zero and 2π. The displacement is the result of a random draw from a Gaussian distribution (Fig. 3.1a) or from an α-stable distribution (Fig. 3.1b). Both the Gaussian walk and the Lévy walk are isotropic, i.e., taken from the center of the circle, all directions are equivalent. A generalization to more than 2 dimensions is

readily formulated and simulated. The random walks then occur inside a ball with a finite radius. Whenever the domain boundary is hit, the particle comes to a standstill. For $\alpha = 2$ the random walk is symmetric under time reversal. However, as was already mentioned in the Introduction, for $0 < \alpha < 2$ the time-reversal symmetry is broken. It is not hard to understand why this is the case. When the particle is followed in forward time, we will often see a Lévy jump that makes the particle come to a standstill at the domain boundary. More rare will be a large jump from the domain boundary into the interior. When a movie of the moving particle is played backward, it will be the other way round. The forward and backward played movie are distinguishable.

Figure 3.2 shows the position distribution that results after a many-step 1D simulation on $-1 \leq x \leq 1$ for $\alpha = 0.8$. For $\alpha = 2$ a flat distribution results. But for $0 < \alpha < 2$ the Lévy jumps that terminate at $x = \pm 1$ and the decreased mobility there lead to an increased probability density near $x = \pm 1$. The Langevin Equation, Eq. (3.3), can be equivalently formulated as a fractional Fokker-Planck equation for the evolution of a probability distribution, i.e. $\partial_t p(x,t) = \sigma^\alpha \partial_x^\alpha p(x,t)$. The stationary distribution is then obtained as the solution of the ordinary differential equation that results when the left hand side is set equal to zero. The fractional derivatives are nontrivial, but in Ref. [86] a solution for the 1D case is presented:

$$p_{st}(x) = \frac{2^{1-\alpha}\Gamma(\alpha)}{\Gamma^2(\alpha/2)} \left(1 - x^2\right)^{\alpha/2-1} , \qquad (3.4)$$

where $\Gamma(.)$ denotes the gamma function. Figure 3.2 shows this solution together with the results of the Langevin simulation. The next section will show with symmetry arguments that the normalized $(1 - r^2)^{\alpha/2-1}$-form generalizes to the nD case, with r being the distance from the center of the ball.
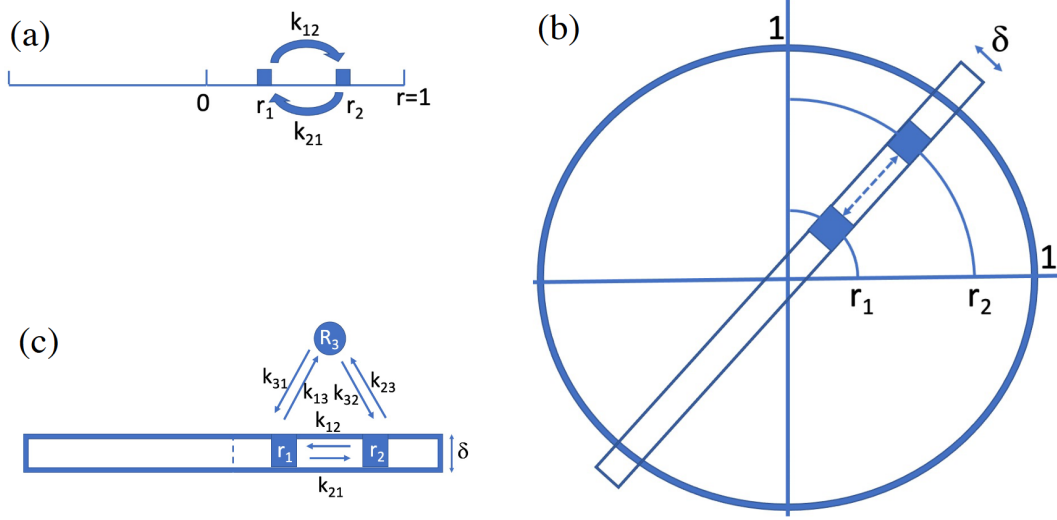
3.3 Extension of the 1D Solution to nD

Figure 3.3: A Lévy walk in a confined domain. Whenever the particle hits the confinement wall, it comes to a standstill there. The 1D steady-state probability distribution (a) is solved in Ref. [86]: $p_{st}(r) \propto (1 - r^2)^{\alpha/2-1}$. Between any two small intervals along the 1D domain, steady state implies $p(r_1)k_{12} = p(r_2)k_{21}$, where the k's denote transition rates. In 2D (b) there is circular symmetry. If we take any narrow bar through the origin and look exclusively at traffic inside that bar, $p_{st}(r) \propto (1 - r^2)^{\alpha/2-1}$ applies again. Next, we take a state R_3 outside the bar (c) and include transitions between r_1 and r_2 that go via any area R_3. As the circular symmetry implies the absence of vortices, transitions k'_{12} and k'_{21} that go via R_3 must also follow $p(r_1)k'_{12} = p(r_2)k'_{21}$. From here it follows that $p_{st}(r) \propto (1 - r^2)^{\alpha/2-1}$ also applies to higher dimensional setups. [2]

For n-dimensions, the stochastic input $\theta_{i,\alpha}$ of Eq. 3.3 is the n-dimensional isotropic stable distribution. This distribution has a a simple characteristic function: $\tilde{\theta}_\alpha(\mathbf{k}) = \exp[-\sigma^\alpha |\mathbf{k}|^\alpha]$. When $\alpha = 2$ this easily reduces to $\tilde{p}_\alpha(\mathbf{k}) = \sum_{d=1}^n \exp[-\sigma k_d^2]$. Each component can be Fourier transformed separately - the variables are independent. Likewise for $\alpha = 2$, the

equivalent Fokker-Planck equation is just Laplace's equation, $0 = \nabla^2 p(\mathbf{x})$, for which the well-known prescription is separation of variables. The solution is just a linear combination of components along each dimension. For $n = 2$ it is $(k_1^2 + k_2^2)^{\alpha/2}$ for example, but for $0 < \alpha < 2$, however, the $|\mathbf{k}|^\alpha$ term cannot be reduced. The individual components of the multivariate stable distribution are *not* statistically independent and the equivalent fractional Fokker-Planck equation cannot be solved by the same means.

Instead, in this section we will use symmetry arguments to show that the 1D steady-state solution generalizes to higher dimensional setups, i.e. an n-dimensional ball of any radius. We will show the solution to have the form $p(r) = C(\alpha)\,(1 - r^2)^{\alpha/2-1}$, where $C(\alpha)$ is the normalization factor (cf. Eq. (3.4)).

First consider the 1D interval depicted in Fig. 3.3a and imagine a large number of particles distributed according to Eq. (3.4). Next take two small intervals on the right side of $r = 0$: $r_1 < r < r_1 + dr$ and $r_2 < r < r_2 + dr$, as depicted. At steady state and within any time interval Δt, there is as much flow from the r_1-interval to the r_2-interval as that there is from the r_2-interval to the r_1-interval, i.e. $J_{12} = J_{21}$. This is detailed balance [87]. Next we define a transition rate, k_{12}, that is the probability per unit of time for a particle in the r_1-interval to transit to the r_2-interval. The rate k_{21} is analogously defined. Detailed balance implies that $k_{12}p(r_1) = k_{21}p(r_2)$ and thus:

$$\frac{k_{12}}{k_{21}} = \frac{p(r_2)}{p(r_1)} = \left(\frac{1 - r_2^2}{1 - r_1^2}\right)^{\alpha/2-1}. \tag{3.5}$$

Next consider the 2D setup depicted in Fig. 3.3b. A bar of width δ is going through the center of the circle. We take two little areas at distances r_1 and r_2 from the center. Consider only trajectories between these two areas that stay within the bar. The traffic inside the bar should mimic the 1D system that was considered in the previous paragraph and Fig. 3.3a. Now consider also the transitions between the two little areas that proceed through trajectories that are not restricted to the narrow bar. Without loss of generality we take an

area R_3, cf. Fig. 3.3c, and we consider trajectories between r_1 and r_2 that pass through R_3.

It is important to realize that the circular symmetry implies that there can be no vortices within the circular domain. Flow along any simple, closed curve within the unit circle would imply that there are points with net flow in the angular direction. So along the r_1, r_2, R_3-loop there need be as much clockwise flow as there is counterclockwise, i.e. $J_{cw} = J_{ccw}$. This implies $k_{12}k_{23}k_{31} = k_{13}k_{32}k_{21}$ [92] and thus:

$$\frac{k_{12}}{k_{21}} = \frac{k_{13}k_{32}}{k_{23}k_{31}}.$$

(3.6)

The "state" R_3 can be taken to be anywhere within the circle and be of any size and shape. We can conclude that the ratio k'_{12}/k'_{21} for transitions along any path between r_1 to r_2 within the circle must be equal to the ratio k_{12}/k_{21} for transitions with trajectories inside the bar.

It follows that, for any dimensionality, the probability density at radius r must be proportional to $(1 - r^2)^{\alpha/2-1}$. For a normalized probability density in n dimensions we derive:

$$p(n, r) = \frac{\Gamma\left(\frac{n+\alpha}{2}\right)}{\pi^{n/2}\Gamma\left(\frac{\alpha}{2}\right)} \left(1 - r^2\right)^{\alpha/2-1}.$$

(3.7)

For $n = 2$ the prefactor reduces to a simple $\alpha/(2\pi)$.

3.4   Two Connected Semicircular Reservoirs

Imagine a semicircular 2D domain with radius R_1 as in Fig. 3.4. There is a small opening with a width d that gives access to a semicircular domain with radius R_2. We have $R_2 < R_1$. Next imagine a large number of particles in this system. The particles are subjected to Lévy noise. In Appendix D it is derived how there is a net flow into the smaller reservoir if both reservoirs have the same homogeneous particle density. So when starting from thermodynamic equilibrium, a higher density develops in the smaller reservoir once Lévy noise starts being applied.
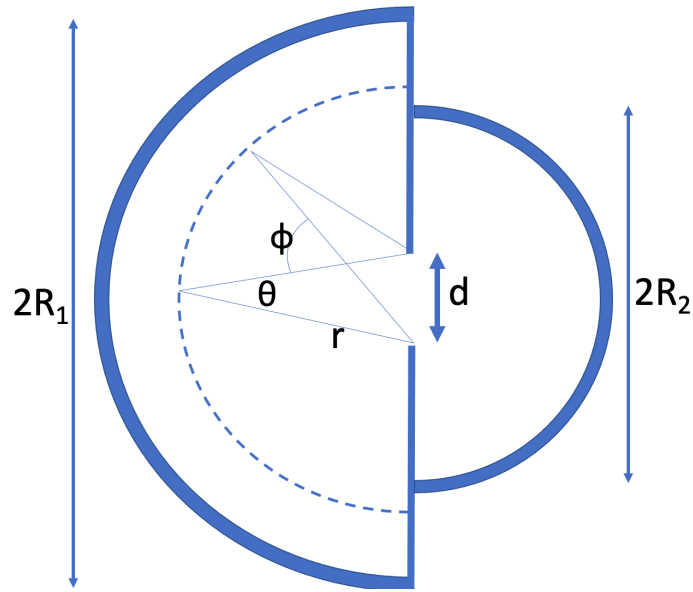
Figure 3.4: Two semicircular reservoirs with a small opening between them. The system contains a large number of noisy particles. At each timestep, each particle moves in an arbitrary direction with a displacement that is drawn from a Gaussian distribution or a Lévy-stable distribution as in Figs. 3.1a and 3.1b. If a particle hits a semicircular wall, it comes to a standstill and only moves again if a computed displacement leads to motion inside the system. If a particle hits the straight vertical wall, it bounces elastically. For Gaussian noise, the system goes to an equilibrium with equal concentration on both sides of the opening. But when the particles are subjected to Lévy noise, the steady state has an accumulation in the smaller reservoir. [2]

3.4.1   Distribution over the Two Reservoirs in Case of Lévy Noise

If the noise in the setup of Fig. 3.4 is Gaussian, then the system will relax to an equilibrium with equal concentration in the two reservoirs. Each particle then has a probability $P_1 = R_1^2/(R_1^2 + R_2^2)$ to be in the larger reservoir and a probability $P_2 = R_2^2/(R_1^2 + R_2^2)$ to be in the smaller reservoir. The probability to be in a certain reservoir is in that case simply proportional to the volume of that reservoir. In 2D the "volume" is the area $V_i = \pi R_i^2/2$.

Next consider Lévy particles. The distribution will now be different. As was shown in the previous section and in Appendix D, Lévy particles tend to accumulate near the walls and in the smaller "nooks and corners." With Lévy particles, the probability to be in the smaller reservoir will be larger than that reservoir's fraction of the total volume.

For a stochastic simulation we let the semicircular walls be "sticky" again, i.e. the particle comes to a standstill upon hitting the wall and only displaces again if a subsequent computed step leads to motion inside the system. If the linear, vertical wall in the middle is hit, an elastic collision occurs. So that wall is "bouncy." An algorithm for treating these boundaries is given in Appendix C.

We will use the 2D solution for a circle, $p_{st}(r) = (\alpha/(2\pi))\,(1 - r^2)^{\alpha/2-1}$, to come to an estimate of the steady-state distribution for the setup in Fig. 3.4. We move to a description where $\rho_i(r_i)$, with $i = 1, 2$, denotes the normalized particle density in reservoir i at a distance r_i from the opening. With

$$\rho_i(r_i) = \frac{\alpha}{\pi R_i^2} \left(1 - \left(\frac{r_i}{R_i} \right)^2 \right)^{\alpha/2-1} \tag{3.8}$$

it is readily verified that

$$\int_{r_i=0}^{R_i} \int_{\phi=-\pi/2}^{\pi/2} \rho_i(r_i) r_i \, dr_i \, d\phi = 1. \tag{3.9}$$

With a large number of particles in the setup, there will be a relaxation to a distribution with a fraction φ_1 in reservoir 1 and a fraction φ_2 in reservoir 2. Obviously we have $\varphi_1 + \varphi_2 = 1$.

For any distribution over the two reservoirs we have:

$$\rho(r_1, r_2) = \varphi_1 \rho_1(r_1) + \varphi_2 \rho_2(r_2). \tag{3.10}$$

It is easy to see that $\int \int \rho(r_1, r_2) = 1$, where the integration is over the entire 2-semicircle system in the figure.

The steady state occurs if there are as many $1 \to 2$ transitions as that there are $2 \to 1$ transitions. We will next derive what values of φ_1 and φ_2 lead to steady state. In the above figure, imagine a semicircular strip of width dr_i at a distance r_i from the opening. The number of particles in the strip is $\rho_i(r_i)\pi r_i dr_i$ $(i = 1, 2)$. We assume that for $r > r_0$, we are in the region where the power-law-description of the tail of the Lévy distribution $(p_\alpha(r) \propto r^{-(\alpha+1)}$ as $r \to \infty)$ applies. The probability that the displacement during one timestep is <u>larger than</u> r is then proportional to $r^{-\alpha}$. For small d and sufficiently large r_0, the angle θ, cf. Fig. 3.4, will be small and we have $d = \theta r$. For a Lévy jump to lead to a particle transiting to the other reservoir, the jump must also be in the right direction. This brings in a factor $(d/r)\cos\phi$, where ϕ is the indicated angle of the position on the semicircle with the horizontal. Integrating over ϕ from $-\pi/2$ to $\pi/2$, the full direction factor is found to be $2d/r$. All in all, during one timestep we have for the number of cross-reservoir transitions from a distance between r and dr:

$$dn_i^{tr}(r_i, r_i + dr_i) \propto \varphi_i \frac{d}{r_i} r_i^{-\alpha} \rho_i(r_i) r_i \, dr_i. \tag{3.11}$$

Integrating from r_0 to the boundary R_i, we obtain for the number of Lévy-jump-associated transitions from reservoir i:

$$N_i^{tr} \propto \frac{\varphi_i}{R_i^2} \int_{r_i=r_0}^{R_i} r_i^{-\alpha} \left(1 - \left(\frac{r_i}{R_i}\right)^2\right)^{\alpha/2-1} dr_i. \tag{3.12}$$

The proportionality constant (associated with the $\propto$) and the r_0 (the radius from which the

power law is taken to describe the Lévy-stable distribution) are the same for both reservoirs. At this point it is also important to realize that for the Lévy jumps to dominate the number of $1 \to 2$ and $2 \to 1$ transitions, R_1 and R_2 must both be much larger than r_0.

Mathematica will readily give an analytical solution for the integral Eq. (3.12). The solution involves the hypergeometric function [93]. Before working out Eq. (3.12) in its full generality, we make a further simplification that will not affect the solution too much: as $R_i \gg r_0$ for both $i = 1$ and $i = 2$, we take $r_0 = 0$ to be the lower limit of the integral. With $0 < \alpha < 1$ the integral will not diverge with $r_i \to 0$. Next, the all-important reservoir radius R_i can be scaled out of the actual integral and incorporated in the prefactor:

$$N_i^{tr} \propto \frac{\varphi_i}{R_i^2} R_i^{-\alpha} R_i \int_{r_i=0}^{R_i} \left(\frac{r_i}{R_i} \right)^{-\alpha} \left(1 - \left(\frac{r_i}{R_i} \right)^2 \right)^{\alpha/2-1} d \left(\frac{r_i}{R_i} \right). \tag{3.13}$$

Upon taking $u = r_i/R_i$ and $v = u^2$ (so $dv = du^2 = 2u\, du$ and thus $du = 1/(2\sqrt{v})\, dv$), further simplification is achieved:

$$N_i^{tr} \propto \varphi_i R_i^{-1-\alpha} \int_{v=0}^{1} v^{-\alpha/2-1/2} \left(1 - v \right)^{\alpha/2-1} dv. \tag{3.14}$$

The integral on the right-hand-side is the well-known Euler integral, which is also known as the beta function [93]. Ultimately, this integral depends only on α. It is finite for $0 < \alpha < 1$ and as it is the same for both reservoirs, we find:

$$N_i^{tr} \propto \varphi_i R_i^{-1-\alpha}. \tag{3.15}$$

The steady state condition is $\varphi_1 R_1^{-1-\alpha} \approx \varphi_2 R_2^{-1-\alpha}$. With $\varphi_1 + \varphi_2 = 1$ we then get:

$$\varphi_1 \approx \frac{R_1^{1+\alpha}}{R_1^{1+\alpha} + R_2^{1+\alpha}}, \quad \varphi_2 \approx \frac{R_2^{1+\alpha}}{R_1^{1+\alpha} + R_2^{1+\alpha}}, \quad \text{and} \quad \frac{\varphi_1}{\varphi_2} \approx \left(\frac{R_1}{R_2} \right)^{1+\alpha}. \tag{3.16}$$

The better approximation is obtained by not fully carrying through the $r_0 = 0$ simpli-

fication of the last paragraph. That the simple approximation according to Eq. (3.16) fails for larger values of α is partly due to scaling issues. For the analytic approximation to be consistent with the numerics, we need $\Delta t^{1/\alpha}$ to be significantly smaller than r_0 (cf. Eq. (3.3) with $\sigma = 1$). Setting $r_0 = 0$ leads to a range where this is no longer true. As α becomes larger, this range becomes larger. Keeping $r_0 > 0$ in Eq. (3.12), we find after some algebra and use of *Mathematica* for the equivalent expression of Eq. (3.15):

$$N_i^{tr} \propto \varphi_i \left[R_i^{-1-\alpha} - \frac{\sqrt{\pi}}{\Gamma(\frac{\alpha}{2})\Gamma(\frac{3-\alpha}{2})} \frac{r_0^{1-\alpha}}{R_i^2} \, _2F_1\left(\frac{1-\alpha}{2}, 1 - \frac{\alpha}{2}; \frac{3-\alpha}{2}; \left(\frac{r_0}{R_i}\right)^2 \right) \right], \qquad (3.17)$$

where $_2F_1(a, b; c; z)$ is the aforementioned hypergeometric function. It is readily verified that the second term in the square brackets dominates for $\alpha \to 2$ and small r_0. This due to the leading $r_0^{1-\alpha}$. The hypergeometric function is defined as a power series [93] and under the $r_0 \ll 1$ condition we can still take $(r_0/R_i)^2 \sim 0$ and hence $_2F_1(.) \approx 1$. The ratio of particles in the two reservoirs is then:

$$\frac{\varphi_1}{\varphi_2} \approx \left(\frac{R_1}{R_2}\right)^{1+\alpha} \frac{\sqrt{\pi} \, R_2^{\alpha-1} - r_0^{\alpha-1}\Gamma(\frac{3-\alpha}{2})\Gamma(\frac{\alpha}{2})}{\sqrt{\pi} \, R_1^{\alpha-1} - r_0^{\alpha-1}\Gamma(\frac{3-\alpha}{2})\Gamma(\frac{\alpha}{2})}, \qquad (3.18)$$

which reduces to $(R_1/R_2)^{1+\alpha}$ (cf. Eq. (3.16)) if we take $\alpha < 1$ and $r_0 \to 0$ concurrently. Note, furthermore, that the equilibrium distribution, i.e. $\varphi_1/\varphi_2 = (R_1/R_2)^2$, is properly approached if we concurrently take $\alpha \to 2$ and $r_0 \to 0$. Both the approximations according to Eq. (3.16) and Eq. (3.18) are depicted in Fig. 3.5 and compared with the results of a stochastic simulation. Finally, it is worth pointing out that Eq. (3.18) is still an approximation. The power law, Eq. (2.8), that characterizes the Lévy-stable distribution is not valid for small values of ξ. For values of ξ near zero, the distribution is Gaussian-like and this is what is relevant for the behavior of particles close to the opening, i.e. $r \to 0$. Gaussian diffusion near the opening will lead to a continuous and differentiable steady-state concentration profile near the opening. This is also what Fig. 3.6 shows.

Figure 3.5 shows the ratio φ_1/φ_2 as a function of α and compares the result of a stochastic
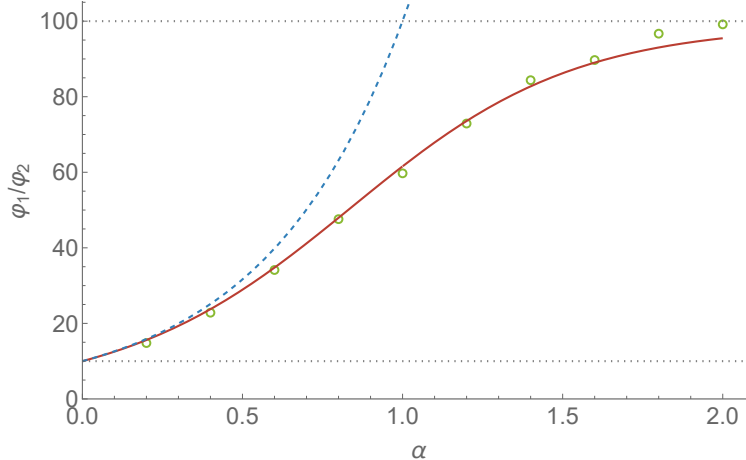
Figure 3.5: For the setup of Fig. 3.4 with $R_1 = 10$ and $R_2 = 1$, we let φ_1 and φ_2 represent the fraction of particles in reservoir 1 and 2, respectively, at steady state. The curves depict the analytic approximations, Eq. (3.16) (dashed) and Eq. (3.18) (solid), of φ_1/φ_2. Each dot is the result of a stochastic simulation of forty thousand particles for 4×10^5 timesteps (with $\Delta t = 0.001$) following a 2×10^5 timestep relaxation period. For the approximation according to Eq. (3.18), we let $r_0 = 0.05$ and find good agreement with the result of the stochastic simulation. [2]

simulation with Eqs. (3.16) and (3.18). We took $R_1 = 10$ and $R_2 = 1$. For $\alpha \to 0$, the simple approximation according to Eq. (3.16) leads to $\varphi_1/\varphi_2 = 10$. For the more sophisticated approximation according to Eq. (3.18), the φ_1/φ_2 value at $\alpha \to 0$ can be brought arbitrarily close to 10 by taking R_1 and R_2 much larger than r_0. There is ten times as much "sticky wall" in the large reservoir and this result tells us that for $\alpha \to 0$ all particles are concentrated at the sticky walls as would intuitively be expected.

The result that is derived in Appendix D hints at the reason that $\alpha = 1$ is "almost like" $\alpha = 2$. As we move away from the opening, the probability to hit the opening decreases as $r^{-\alpha}$. However, with a homogeneous distribution of particles, the number of particles at a distance between r and $r + dr$ increases proportional to r. For an n-dimensional setup, the increase is proportional to r^{n-1} (for $n = 2$ we have circular strips and for $n = 3$ we have spherical shells). All in all, we find that the number of "hits" from a distance r is proportional to $r^{n-\alpha-1}$. Note that for $n = 3$, the entire range of α leads to an increase of "hits" with r. We have not done any further investigation of the 3D case. We see that for
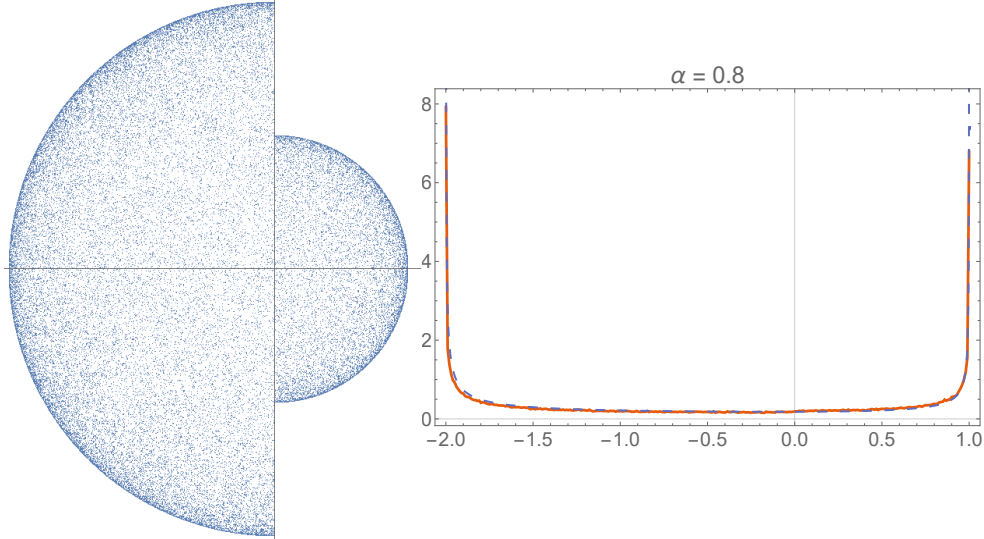
Figure 3.6: The figure on the left depicts a steady-state distribution for fifty thousand Lévy particles in a two-reservoir confinement as depicted in Fig. 3.4 after 10^5 timesteps. We have $R_1 = 2$, $R_2 = 1$, $\alpha = 0.8$, and the opening has a width $d = 0.1$. For the figure on the right we started with a steady-state distribution and ran the simulation for another 10^5 iterations. We took a horizontal strip through the center with a width of 0.02 and partitioned it into 300 bins. Particles in each bin were counted and the results of the subsequent 10^5 iterations were added. The solid line represents the resulting normalized 1D histogram. The dashed reference curve is the solution Eq. (3.4). For the left reservoir the domain was scaled to a length 2. Normalization of the combination of analytic solutions was done such that the probability to be in the left reservoir is 2/3. It is readily verified that this leads to continuity at the location of the opening. [2]

$n = 2$, an increase of "hits" with r only occurs if $\alpha < 1$. For $1 < \alpha < 2$, the number of "hits" decreases with r and in that case transitions mostly happen from the region around the opening. This decrease with $1 < \alpha < 2$ also means that the particle exchange through the opening does not "feel" the different radii of the different reservoirs anymore. Equation (3.4) describes and Fig. 3.6 shows a nonhomogeneous distribution: as we move away from the opening, the concentration actually increases. This should add to the exponent $n - \alpha - 1$ that we derived in this paragraph. Some of this effect is incorporated in the approximation that led to Eq. (3.18). Both that approximation and the simulations show an asymptotic approach to $(R_1/R_2)^2$ as $\alpha \to 2$ and $r_0 \to 0$.

3.4.2 Entropies and Energies Associated with Lévy Noise

The nonhomogeneous distributions shown in Figs. 3.2 and 3.6 essentially function as dissipative structures [91]. The depicted nonhomogeneous steady-state distributions represent a lower entropy than homogeneous distributions. But these lower-entropy structures facilitate the transfer and dissipation of energy at steady state. The transferred energy comes in through the non-thermal motion of the active particles. One can conceive of this energy then being dissipated to the media and released through the boundaries of the system. Under such a conception, the accumulation of the active particles near the boundary would help facilitate this process. Those dynamics are not here explored, but are mentioned to illustrate how, ultimately, the low-entropy dissipative structures help the energy throughput and the entropy production.

Because of the divergent standard deviation of the α-stable noise, the energy that is dissipated per unit of time is in principle infinite. The finite container size, however, truncates the Lévy jumps and make the aforementioned standard deviation of the jump sizes finite. We will not elaborate on this. What we will instead focus on in this subsection is the entropy decrease that is associated with the apparent nonhomogeneous distribution shown in Fig. 3.6.

Imagine that the steady flow of energy that maintains the dissipative structure is suddenly halted, i.e. the noise becomes Gaussian in Eq. 3.3 ($\theta_{\alpha,i} \rightarrow \theta_{2,i}$). Such halting is straightforward if the active-particle-motion is, for instance, driven by magnetic forces or by optics. The distribution in Fig. 3.6 will then homogenize. Such homogenization implies an increase in entropy and a concurrent decrease in free energy. Below we will find remarkably concise analytic expressions for the entropy change.

The relaxation towards homogeneity is two-part. First there is an intra-reservoir relaxation inside each of the two reservoirs to a spatially homogeneous spread. Next there is the slower relaxation between the two reservoirs towards a ratio $\varphi_1/\varphi_2 = V_1/V_2 = R_1^2/R_2^2$.

The entropy change associated with the intra-reservoir relaxations is hard to compute

for the semicircular reservoirs of Figs. 3.4 and 3.6. But for a circular reservoir as in Fig. 3.1 it is easier and no resort to numerics is necessary. We take the 2D solution of Eq. 3.7, $p_{ini}(r) = (\alpha/2\pi)(1 - r^2)^{\alpha/2-1}$, as the initial distribution and $p_{fin}(r) = 1/\pi$ as the final homogeneous distribution. It is well-known that for a discrete set of probabilities, p_i, the associated entropy is given by $S = -\Sigma_i p_i \log p_i$. However, this summation cannot be straightforwardly extended to an integral for the case of a continuous probability density $p(r)$. An obvious issue is that density is not dimensionless and that a logarithm can only be taken of a dimensionless quantity. In Ref. [94] it is explained how a sensible definition is only obtained after introducing another probability density that functions as a measure. We then obtain what is known as the relative entropy or Kullback-Leibler divergence [88]:

$$D_{\mathrm{KL}}(p_{fin}||p_{ini}) = \int_{r \leq 1} p_{fin}(r) \log \left(\frac{p_{fin}(r)}{p_{ini}(r)} \right) dr. \tag{3.19}$$

With the above expressions for $p_{ini}(r)$ and $p_{fin}(r)$, we find after some algebra that $D_{\mathrm{KL}}(p_{fin}||p_{ini}) = -1 + \alpha/2 + \log(2/\alpha)$. No such easy analytic solution ensues for more than two dimensions or even in the 1D case. The Kullback-Leibler divergence can be thought of as a kind of distance between two probability densities. However, it is generally not symmetric in the two involved distributions. In our case, we find $D_{\mathrm{KL}}(p_{ini}||p_{fin}) = -1 + 2/\alpha + \log(\alpha/2)$. Both $D_{\mathrm{KL}}(p_{fin}||p_{ini})$ and $D_{\mathrm{KL}}(p_{ini}||p_{fin})$ are remarkably simple expressions; they are continuous and concave up as α increases and reduce to zero for $\alpha = 2$.

The speed of the inter-reservoir relaxation depends on the size of the opening. For the small opening that is necessary for our approximations to be accurate, it will generally be slower than the intra-reservoir relaxation. For the inter-reservoir relaxation the basic quantity is the probability to be in either of the two reservoirs. We go back to the basics to calculate what the entropy is for a given distribution over the two reservoirs.

In the Statistical Physics context, entropy is commonly defined as proportional to the logarithm of the number of microstates [87]. Imagine that there are N identical particles in

the setup of Figs. 3.4 and 3.6. Here N is taken to be very large. In case of equilibrium the number of particles in a reservoir is proportional to the volume $V_i = \pi R_i^2/2$ of a reservoir. With $\varphi_i N$ identical particles in reservoir i, the number of microstates in each of the two reservoirs is given by:

$$\Omega_i = \frac{V_i^{\varphi_i N}}{(\varphi_i N)!}. \tag{3.20}$$

The numerator has the $\varphi_i N$-exponent because it is for each particle that the number of microstates is proportional to the volume. The microstate is the same, however, when two or more particles are exchanged. The denominator takes this into account and denotes the number of permutations among $\varphi_i N$ particles. With the definition $S = \log \Omega$ and using Stirling's approximation [87] ($\log N! = N \log N$, if N is very large), we derive

$$S_i = \varphi_i N \log \left(\frac{V_i}{\varphi_i N} \right), \tag{3.21}$$

where "log" denotes the natural logarithm. As was mentioned before, at thermodynamic equilibrium the fraction of particles in a reservoir is proportional to the volume of that reservoir, i.e., $\varphi_i \propto V_i$. The argument of the logarithm in Eq. (3.21) is then the same constant for both reservoirs. This leads to $S_i \propto \varphi_i$, as should be expected from an equilibrium-thermodynamics perspective.

We take for the total volume and the total entropy $V_{tot} = V_1 + V_2$ and $S_{tot} = S_1 + S_2$, respectively. It is next derived from Eq. (3.21) that $S_{tot} = N \left(\varphi_1 \log \left(V_1/\varphi_1 \right) + \varphi_2 \log \left(V_2/\varphi_2 \right) \right) - N \log N$. The additive $N \log N$-term is the same for all values of α. As it is only differences in entropy that matter, we discard this term. For the entropy per particle, $s_{tot} = S_{tot}/N$, it is next found:

$$s_{tot} = \varphi_1 \log \left(\frac{V_1}{\varphi_1} \right) + \varphi_2 \log \left(\frac{V_2}{\varphi_2} \right). \tag{3.22}$$

Figure 3.7 depicts s_{tot} as a function of α following Eq. (3.22). We took $V_{tot} = 1$ (leading to $V_1 = R_1^2/(R_1^2 + R_2^2)$ and $V_2 = R_2^2/(R_1^2 + R_2^2)$) and $R_1 = 10R_2$. For the dashed curve Eq. (3.16) was used to come to the values of φ_1 and φ_2. For the solid curve the improved approximation,
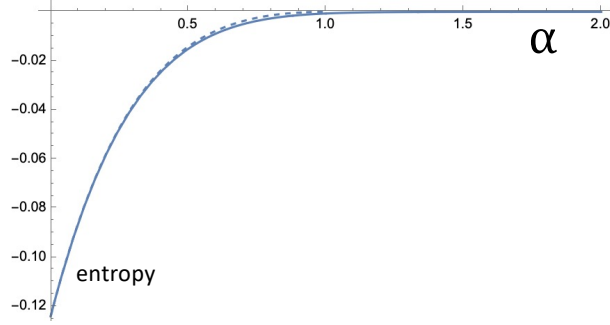
Figure 3.7: Given the setup of Fig. 3.4 with $V_{tot} = 1$ and $R_1 = 10R_2$, the curves show the entropy per particle, s_{tot}, as a function of the stability parameter α of the Lévy noise. The nonequilibrium noise leads to a concentration difference between the two reservoirs. The associated entropy decrease s_{tot} is obtained by substituting into Eq. (3.22) the approximate ratio according to Eq. (3.16) (dashed curve) and according to Eq. (3.18) (solid curve). For Eq. (3.18) we took $r_0 = 0.05$., i.e. the value that led to good agreement with the stochastic stimulation (cf. Fig. 3.5). [2]

Eq. (3.18), was used with $r_0 = 0.05$. The curves appear almost indistinguishably close. It is important to realize that this entropy also represents free energy. The free energy release associated with the equilibration can be obtained by multiplying the entropy (cf. Eq. (3.22)) with the temperature of the environment.

There is a more thermodynamic way to derive the right hand side of Eq. (3.22) through the energy per particle that would be invested in building the dissipative structure. With intra-reservoir equilibrium established, the chemical potential μ that is driving flux through the opening is the logarithm of the concentration ratio [87]. If we let ϕ be the fraction of the particles in the smaller reservoir during this construction, then we have $\mu(\phi) = \log\left(\frac{\phi}{V_2}\right) - \log\left(\frac{1-\phi}{V_1}\right)$. The energy that is dissipated when an infinitesimal fraction $d\phi$ follows the potential and flows through the opening is $\mu(\phi)\, d\phi$. The entire equilibration takes ϕ from the starting nonequilibrium fraction φ_2 to the final equilibrium fraction V_2. After some algebra and setting the temperature and the Boltzmann constant all equal to unity, it is found that the resulting total-equilibration-energy integral reduces to $-s_{tot}$ (cf. Eq. (3.22)).

Equations (3.16) and (3.22) are concise and intuitive. Equation (3.16) is already a fairly accurate approximation. Given the geometry of the system and the value of α, Eq. (3.16)

73

gives the distribution over the two reservoirs. Equation (3.22) tells us what entropy decrease and what free energy "investment" is associated with the concentration difference between the reservoirs that gets established due to the active particle movement. It gives a measure for how far the system is driven from equilibrium by the active particle motion.

Chapter 4

Conclusion

A thorough understanding of the universe will require a thorough understanding of nonequilibrium. Such an understanding is still far off. It is still not entirely clear when we should shift our framework of analysis from equilibrium to nonequilibrium. This work represents a modest exploration in that direction in the context of stable noise-driven processes.

Chapter 2 develops a parameter, $0 < r < 1$ (cf. Eq. (2.39)), cast in the form of an order parameter which quantifies the breaking of microscopic reversibility. We took a basic and generic system: a noisy, overdamped particle in a parabolic potential. It was shown how the degree of symmetry breaking depended on both the stability index α of the noise as well as the choice of time interval Δt for the simulation. For $\alpha = 2$ there is Gaussian noise, yielding time-reversal symmetry and $r = 0$. The symmetry breaking increases as one moves toward $\alpha = 0$. Fig. 2.12 shows the dependence on Δt and this is ultimately what allows possible analysis of real systems for which the sampling rate is in some sense arbitrary.

Through the use of the parameter r we overcome some of the difficulties that are ordinarily faced in the estination of the stability index α. Several of the methods rely on the assumption that the amplitude of the noise is constant throughout the signal which often requires one to segment or discard portions of data. Such is the case for x-ray fluxes from the sun which follow an ≈ 11 year cycle. Our method is insensitive to such changes in scale. It is

furthermore remarkable and useful that the value of r stays the same when the time signal that is being followed is not the x in Eq. (2.6), but an odd or even function $f(x)$ where $f'(x) > 0$ for $x > 0$. The value of r readily leads to the stability index α that characterizes the underlying Lévy noise term $\xi_\alpha(t)$ (cf. Eq. (2.6)). A good estimate for α is essential in identifying the physics taking place at the source of a signal. The method developed in Section 2.4.3 yields a reliable estimate of α from a real-life time series. This method could more generally be helpful in the analysis of nonequilibrium systems, not just in astrophysics, but also in geology, physiology, climate science, economics, etc.

Chapter 3 investigates the consequences of a bath in which particle velocities are Lévy-stable distributed. In such a system, larger concentrations of particles occur near the walls and in smaller cavities. We have analytic expressions for the distribution of Lévy particles in the circular and the spherical domain. For the two connected reservoirs as depicted in Fig. 3.4, we have derived a good approximation for the concentration difference between the reservoirs at steady state. We have presented an accounting of the energies and entropies for such divergence from equilibrium.

This work may have implications for a number of different fields. The initial discussion honed in on active particles and how e.g. bacteria will accumulate in regions of high curvature [95]. It has also already been demonstrated that fluids containing bacteria or other active particles can lead to interesting and unexpected hydrodynamics, including Lévy-like, for *passive* particles in the same liquid [96, 31].

There may also be a connection with plasma physics, where it is still common to assume particle speeds follow a Maxwell-Boltzmann distribution [87]. There is some evidence that this *equilibrium* assumption may not be adequate. At Lawrence Livermore Lab a table-top-size construction was developed to generate pulses of fast neutrons from high-energy deuterium collisions in plasma. Such collisions lead to the nuclear reaction D+D $\rightarrow^3$He + n [97]. In the experiments it appears that the number of produced neutrons exceeds the theoretical predictions by more than an order of magnitude. Plasmas in which energy is

converted or transferred are of course not in a thermodynamic equilibrium. In containers with plasma, a homogeneous distribution is therefore unlikely and accumulation at the edge as described in this work is possible. This is important because it means that fusion reactions in a plasma will occur at different rates at different positions. Through feedback mechanisms such inhomogeneities may rapidly augment and possibly develop into serious instabilities.

Engineered microswimmers are probably the field where our results could ultimately be most applicable. There are good methods and technologies for manipulating suspended micrometer size particles from the outside with acoustic, magnetic or optic signals (see e.g. Refs. [98] and [99]). Today the exciting new developments are in the medical application of such microrobots. Clinical uses for imaging, sensing, targeted drug delivery, microsurgery, and artificial insemination are envisaged and researched [100]. The microswimmers and microrobots are particles that are operating in a very noisy environment. Accumulations as described and explained in this article are likely to be encountered.

There appears to be a connection between nonequilibrium and alpha stable noise. The investigation in the last two chapters provides a subtle clue. Richard Feynman was invoked in the Introduction to help explain the implicit scale in the assumption of equilibrium. Nothing is truly at equilibrium, but on the physical scale of a laboratory and the time scale of the experimenter it is a good approximation. Lévy noise, however, has no scale. If it is present in a system, it can make itself known regardless of the window of observation.

The analysis of solar flare data in Section 2.4.3, included as an implementation of the α parameter, demonstrates that idea. A Lévy walk ordinarily has no identifiable 'arrow of time', but the presence of a potential can break this symmetry. This potential imposes a timescale upon the system and when we view the system at similar scales we find the largest breaking of symmetry. What is the chance that the structure of the noise is relevant in precisely those ranges? With Lévy noise, it is a certainty. The structure of Lévy noise has a fractal character and appears the same when viewed on any scale. Likewise in the behavior of the reservoir system of Section 3.4. The accumulation of active particles has

prior been modeled with Gaussian noise by assuming that noise must have a very large amplitude [84]. No such assumptions are necessary in our case. The elegance of our results here are owed entirely to the elegance of Lévy distributions. Some may oppose the use of Lévy noise on the grounds that its infinite variance is unphysical. However, nothing particularly unphysical has emerged from its use in these model systems. What emerges instead are structures reminiscent of the 'dissipative structures' of Prigogine in which systems spontaneously organize to facilitate the transport of energy and production of entropy.

References

[1] S. Yuvan and M. Bier, Physical Review E **104**, 014119 (2021).

[2] S. Yuvan and M. Bier, Entropy **24**, 189 (2022).

[3] P. Bełdowski et al., Chemistry and physics of lipids **216**, 17 (2018).

[4] S. Yuvan, N. Bellardini, and M. Bier, Symmetry **14** (2022).

[5] P. Raczyński, K. Górny, P. Bełdowski, S. Yuvan, and Z. Dendzik, The Journal of Physical Chemistry B **124**, 6592 (2020).

[6] P. Bełdowski, S. Yuvan, A. Dėdinaitė, P. M. Claesson, and T. Pöschel, Colloids and Surfaces B: Biointerfaces **184**, 110539 (2019).

[7] B. Lisowski, S. Yuvan, and M. Bier, Biosystems **177**, 16 (2019).

[8] S. Yuvan and M. Bier, Sense and nonsense about water, in Water in biomechanical and related systems, pages 19–36, Springer, 2021.

[9] P. Raczyński et al., Sensors **21**, 7011 (2021).

[10] S. Yuvan and M. Bier, Physics Letters A **382**, 367 (2018).

[11] S. Yuvan and M. Bier, Physics of Biological Oscillators: New Insights into Non-Equilibrium and Non-Autonomous Systems , 131 (2021).

[12] S. A. Hollingsworth and R. O. Dror, Neuron **99**, 1129 (2018).

[13] W. Jia et al., Pushing the limit of molecular dynamics with ab initio accuracy to 100 million atoms with machine learning, in <u>SC20: International Conference for High Performance Computing, Networking, Storage and Analysis</u>, pages 1–14, IEEE, 2020.

[14] R. P. Feynman, <u>Statistical mechanics: a set of lectures</u>, CRC press, 2018.

[15] I. Prigogine, Science **201**, 777 (1978).

[16] D. S. Lemons, An introduction to stochastic processes in physics, 2003.

[17] S. F. Gull, Bayesian inductive inference and maximum entropy, in <u>Maximum-entropy and Bayesian methods in science and engineering</u>, pages 53–74, Springer, 1988.

[18] B. Mandelbrot, The Journal of Business **36**, 349 (1963).

[19] R. K. Pathria and P. D. Beale, 6 - The Theory of Simple Gases, in <u>Statistical Mechanics (Third Edition)</u>, edited by R. K. Pathria and P. D. Beale, pages 141–178, Academic Press, Boston, third edition edition, 2011.

[20] L. Onsager, Phys. Rev. **37**, 405 (1931).

[21] L. Onsager, Phys. Rev. **38**, 2265 (1931).

[22] L. Onsager and S. Machlup, Physical Review **91**, 1505 (1953).

[23] M. Bier and R. D. Astumian, Physics Letters A **247**, 385 (1998).

[24] M. Bier, I. Derényi, M. Kostur, and R. D. Astumian, Physical Review E **59**, 6422 (1999).

[25] V. M. Zolotarev, <u>One-dimensional stable distributions</u>, volume 65, American Mathematical Soc., 1986.

[26] B. Mandelbrot, <u>The fractal geometry of nature</u>, volume 1, WH Freeman, San Francisco, 1983.

[27] C. K. Peng et al., Physical review letters **70**, 1343 (1993).

[28] M. Rypdal and K. Rypdal, Phys. Rev. Lett. **104**, 128501 (2010).

[29] P. D. Ditlevsen, Phys. Rev. E **60**, 172 (1999).

[30] K. Burnecki, A. Wyłomańska, A. Beletskii, V. Gonchar, and A. Chechkin, Phys. Rev. E **85**, 056711 (2012).

[31] K. Kanazawa, T. G. Sano, A. Cairoli, and A. Baule, Nature **579**, 364 (2020).

[32] B. Dybiec, E. Gudowska-Nowak, and I. Sokolov, Physical Review E **78**, 011117 (2008).

[33] N. G. Van Kampen, Stochastic processes in physics and chemistry, volume 1, Elsevier, 1992.

[34] M. Muller, Annals of Mathematical Statistics **29**, 610 (1958).

[35] K. Górska and K. A. Penson, Physical Review E **83**, 061125 (2011).

[36] J. M. Chambers, C. L. Mallows, and B. Stuck, Journal of the american statistical association **71**, 340 (1976).

[37] R. Weron, Statistics & probability letters **28**, 165 (1996).

[38] M. Veillette, STBL: Alpha stable distributions for MATLAB, Retrieved July 20, 2020.

[39] E. Pantaleo, P. Facchi, and S. Pascazio, Physica Scripta **2009**, 014036 (2009).

[40] R. Metzler and J. Klafter, Physics reports **339**, 1 (2000).

[41] J. Moyal, Journal of the Royal Statistical Society. Series B (Methodological) **11**, 150 (1949).

[42] R. Metzler, E. Barkai, and J. Klafter, EPL (Europhysics Letters) **46**, 431 (1999).

[43] H. C. Fogedby, Physical Review E **50**, 1657 (1994).

[44] V. Yanovsky, A. Chechkin, D. Schertzer, and A. Tur, Physica A: Statistical Mechanics and its Applications **282**, 13 (2000).

[45] D. Brockmann and I. Sokolov, Chemical Physics **284**, 409 (2002).

[46] E. C. De Oliveira and J. A. Tenreiro Machado, Mathematical Problems in Engineering **2014** (2014).

[47] F. Liu, V. Anh, and I. Turner, Journal of Computational and Applied Mathematics **166**, 209 (2004).

[48] M. M. Meerschaert and C. Tadjeran, Applied numerical mathematics **56**, 80 (2006).

[49] M. Kateregga, S. Mataramvura, and D. Taylor, Cogent Economics & Finance **5**, 1318813 (2017).

[50] G. Muñoz-Gil et al., Nature communications **12**, 1 (2021).

[51] J. H. McCulloch, Communications in Statistics-Simulation and Computation **15**, 1109 (1986).

[52] W. H. Press, B. P. Flannery, S. A. Teukolsky, and W. T. Vetterling, Numerical recipes in FORTRAN: The art of scientific computing), chapter 15, pages 695–697, Cambridge Univ. Press, Cambridge, 1992.

[53] J. P. Nolan, Maximum likelihood estimation and diagnostics for stable distributions, in Lévy processes, pages 379–400, Springer, 2001.

[54] H. E. Hurst, Transactions of the American society of civil engineers **116**, 770 (1951).

[55] R. Metzler, J.-H. Jeon, A. G. Cherstvy, and E. Barkai, Physical Chemistry Chemical Physics **16**, 24128 (2014).

[56] M. Magdziarz, A. Weron, K. Burnecki, and J. Klafter, Physical review letters **103**, 180602 (2009).

[57] M. Magdziarz and J. Klafter, Physical Review E **82**, 011129 (2010).

[58] K. Burnecki and A. Weron, Physical Review E **82**, 021130 (2010).

[59] N. Kruszewska et al., Energies **12**, 3448 (2019).

[60] I. Wong et al., Physical review letters **92**, 178101 (2004).

[61] F. Amblard, A. C. Maggs, B. Yurke, A. N. Pargellis, and S. Leibler, Physical review letters **77**, 4470 (1996).

[62] I. Mahmad Rasid, N. Holten-Andersen, and B. D. Olsen, Macromolecules **54**, 1354 (2021).

[63] J.-H. Jeon and R. Metzler, Journal of Physics A: Mathematical and Theoretical **43**, 252001 (2010).

[64] M. Islam, Physica Scripta **70**, 120 (2004).

[65] A. Einstein, Annalen der physik **4**, 549 (1905).

[66] V. M. v. Smoluchowski and I. D. im unbegrenzten Raum, Ann. d. Phys **21**, 756 (1906).

[67] H. Risken, Fokker-planck equation, in The Fokker-Planck Equation, pages 63–95, Springer, 1996.

[68] L. Fletcher et al., Space science reviews **159**, 19 (2011).

[69] E. N. Parker, The Astrophysical Journal **330**, 474 (1988).

[70] E. N. Parker, Solar and stellar magnetic fields and atmospheric structures: Theory, in International Astronomical Union Colloquium, volume 104, pages 271–288, Cambridge University Press, 1989.

[71] N. B. Crosby, M. J. Aschwanden, and B. R. Dennis, Solar Physics **143**, 275 (1993).

[72] A. A. Stanislavsky, K. Burnecki, M. Magdziarz, A. Weron, and K. Weron, The Astrophysical Journal **693**, 1877 (2009).

[73] S. A. Stoev, G. Michailidis, and M. S. Taqqu, IEEE Transactions on Information Theory **57**, 1615 (2011).

[74] S. Das, G. Gompper, and R. G. Winkler, New Journal of Physics **20**, 015001 (2018).

[75] E. M. Purcell, American journal of physics **45**, 3 (1977).

[76] J. Klafter, M. F. Shlesinger, and G. Zumofen, Physics today **49**, 33 (1996).

[77] P. Lévy, Calcul des probabilités,, Gauthier-Villars, Paris, 1925.

[78] G. Samorodnitsky and M. S. Taqqu, Stable Non-Gaussian Random Processes: Stochastic Models with Infinite Variance: Stochastic Modeling, Chapman & Hall, London, UK, 1994.

[79] E. Milotti, arxiv (2002).

[80] P. A. Abrams, The American Naturalist **124**, 80 (1984).

[81] A. Mårell, J. P. Ball, and A. Hofgaard, Canadian Journal of Zoology **80**, 854 (2002).

[82] C. T. Brown, L. S. Liebovitch, and R. Glendon, Human Ecology **35**, 129 (2007).

[83] S. M. Pikkujämsä et al., Circulation **100**, 393 (1999).

[84] Y. Fily, A. Baskaran, and M. F. Hagan, Soft matter **10**, 5609 (2014).

[85] S. Jespersen, R. Metzler, and H. C. Fogedby, Physical Review E **59**, 2736 (1999).

[86] S. I. Denisov, W. Horsthemke, and P. Hänggi, Physical Review E **77**, 061112 (2008).

[87] R. W. Schwenz and R. J. Moore, Physical Chemistry, Longman, London, 1972.

[88] S. Kullback and R. A. Leibler, The annals of mathematical statistics **22**, 79 (1951).

[89] S. Hermann and M. Schmidt, Communications Physics **4**, 1 (2021).

[90] N. Kadkhoda et al., Symmetry **12**, 1282 (2020).

[91] D. Kondepudi and I. Prigogine, Modern Thermodynamics: From Heat Engines to Dissipative Structures, 1998.

[92] T. L. Hill, Free energy transduction and biochemical cycle kinetics, Dover Publications, New York, 2004.

[93] M. Abramowitz and I. A. Stegun, Handbook of mathematical functions with formulas, graphs, and mathematical tables, Dover Publications, New York, 1965.

[94] E. T. Jaynes, Information theory and statistical mechanics, in Statistical Physics—1962 Brandeis Summer Institute Lectures in Theoretical Physics, Vol. 3, pages 181–218, Benjamin, New York, 1963.

[95] P. Galajda, J. Keymer, P. Chaikin, and R. Austin, Journal of bacteriology **189**, 8704 (2007).

[96] O. Sipos, K. Nagy, R. Di Leonardo, and P. Galajda, Physical review letters **114**, 258104 (2015).

[97] J. Zweiback et al., Physical review letters **85**, 3640 (2000).

[98] H.-R. Jiang, N. Yoshinaga, and M. Sano, Physical review letters **105**, 268302 (2010).

[99] X. Peng et al., Light: Science & Applications **9**, 1 (2020).

[100] A.-I. Bunea and R. Taboryski, Micromachines **11**, 1048 (2020).

[101] F.-T. Frerichs, Friedrich Vieweg und Sohn: Braunschweig, Germany , 463 (1846).

[102] B. Zappone, M. Ruths, G. W. Greene, G. D. Jay, and J. N. Israelachvili, Biophysical journal **92**, 1693 (2007).

[103] G. D. Jay and K. A. Waller, Matrix Biology **39**, 17 (2014).

[104] C. Rimington, Annals of the rheumatic diseases **8**, 34 (1949).

[105] D. P. Chang et al., Soft Matter **5**, 3438 (2009).

[106] J. M. Coles, D. P. Chang, and S. Zauscher, Current Opinion in Colloid & Interface Science **15**, 406 (2010).

[107] R. V. Pai, J. D. Monpara, and P. R. Vavia, Journal of Controlled Release **309**, 190 (2019).

[108] K. L. Rhinehardt, G. Srinivas, and R. V. Mohan, The Journal of Physical Chemistry B **119**, 6571 (2015).

[109] J. Lesitha Jeeva Kumari, R. Jesu Jaya Sudan, and C. Sudandiradoss, PloS one **12**, e0183041 (2017).

[110] J. An et al., Langmuir **33**, 4386 (2017).

[111] L. A. Abriata, E. Spiga, and M. Dal Peraro, Biophysical journal **111**, 743 (2016).

[112] E. A. Cino, M. Karttunen, and W.-Y. Choy, PLoS One **7**, e49876 (2012).

[113] C. Echeverria and R. Kapral, Physical Chemistry Chemical Physics **14**, 6755 (2012).

[114] B. Macao, D. Johansson, G. Hansson, and T. Hard, Nat. Struct. Mol. Biol **13**, 71 (2006).

[115] Y. Duan et al., Journal of computational chemistry **24**, 1999 (2003).

Appendix A

Mucin Simulation Description

There is evidence that phase transition-like effects and nonequilibrium phenomena may play an important role in some dynamic biological systems, particularly network formation. One key player in this respect are the mucins. Mucins are large glycoproteins first isolated by acetic acid precipitation - little more than mixing joint fluid with the acidic component of vinegar - as early as 1846 by German pathologist Frerichs [101]. They are widely distributed in the human body - they can be found in the stomach, lungs, respiratory tract, gastrointestinal tract, liver, kidney, colon, eye, and ear [102]. They lubricate and protect a large range of epithelial surfaces by forming gel-like mucosae when secreted in a large enough concentration. There are also mucin-like regions present in other molecules known for their lubricating properties, such as lubricin [103, 104] - suggested to be the key constituent in Frerich's joint fluid, i.e. synovial fluid [105]. Lubricin itself is too complex a molecule (comprised of over 1400 amino acids) with too many glycosilation sites to model realistically.

Genetic sequencing has identified 22 human mucin genes, denoted MUC1-MUC22. Here MUC1 is studied as it is the most widely distributed in humans and contains the features of the mucin family responsible for lubricating properties [106]. Prior studies of mucin's docking/binding and adhesive properties [107, 108, 109, 110] have targeted inter-molecular hydrogen bonds as being of principal importance in its biological function. How mucins

cross-link to form networks and the statistical nature of the atomic interactions will be discussed.

In vivo, proteins operate in crowded environments [111]. It is obvious and intuitive that this will affect behavior. In [112] it was shown that the excluded volume effect, produced by a high density of macromolecules, alters the stability and the folding rate of globular proteins. This is because the macromolecules do not have the same freedom to explore all of their possible conformations as they would in an uncrowded environment. Instead they entropically tend toward more compact states that 'exclude' less volume from the system as a whole.

The difference between crowded and diluted environments can be observed in the inter- and intra-molecular interactions, especially in hydrogen bonds' creation and annihilation, and the hydrophobic interactions, which are of major importance for self-arrangement and dynamic properties. Molecular crowding also affects the transport properties of proteins; molecules in a crowded system exhibit subdiffusion [113]. Molecular dynamics is able to probe both of these effects by calculating bond energies based on an implemented potential, and creating statistical ensemble averages over the course of many simulations.

A visualization of MUC1, whose structure was retrieved from the Protein Data Bank [114], is shown in Fig. A.1. A molecular dynamics simulation of a fixed size allows only relatively coarse control over the concentration of protein molecules. In these simulations, even adding a single mucin molecule represents an increased concentration of about 10.68 g/L, but this is not the main limitation. What actually bottlenecks the resolution of the study is simulation time. Each chosen concentration was simulated 20 times with randomized realizations of temperature to obtain a reliable average. Because of this, and the large range of concentrations to probe, increments of five mucin molecules were used for five concentrations, from $c_1 = 53.42$ g/L (5 mucin molecules) to $c_5 = 267.1$ g/L (25 mucin molecules). This encompasses the range present in living organisms and provides both under- and over-crowded conditions.
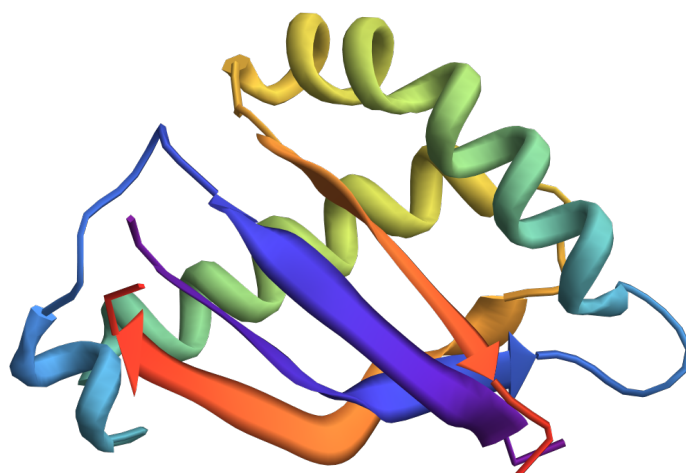
Figure A.1: Ribbon diagram of MUC1 visualized with *Mathematica*. It is a complex of two separate chains, connected by their interleafed β-strands.
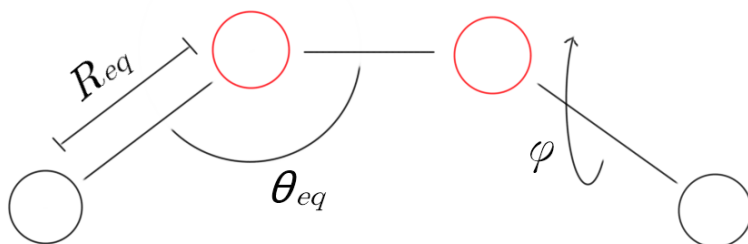
Figure A.2: Depiction of the equilibrium bond parameters from Eq. A.1.

Molecular dynamics simulations are deterministic. The evolution of a system from its initial conditions is determined by a user defined 'force field', of which there are numerous standards, that defines the potential energy of a particular arrangement of atoms. At each time step, the atoms in the simulation move toward the lowest energy configuration possible. For protein simulation, the AMBER force field is widely used and trusted. The AMBER03

force field [115] is given by:

$$E_{total} = \sum_{bonds} k_b(R - R_{eq})^2 + \sum_{angles} k_\theta(\theta - \theta_{eq})^2 +$$

$$\sum_{dihedrals} \frac{V_n}{2}[1 + \cos(n\phi - \gamma)] + \sum_{i<j} \left[\frac{A_{ij}}{R_{ij}^{12}} - \frac{B_{ij}}{R_{ij}^6} + \frac{q_i q_j}{\epsilon R_{ij}} \right], \quad (A.1)$$

where k_b, k_θ, and V_n are force constants. The various atomic bonds are incorporated based on known equilibrium lengths R_{eq} and angles θ_{eq}. Thus the first two sums represent the approximate energy cost of deviating from these known equilibrium values. The third sum represents a torsion term for dihedrals, with torsion angle ϕ, multiplicity n, and a phase value γ of 0° or 180°. These are arrangements of four atoms for which the central bond can be 'twisted', see Fig. A.2. The final sum accounts for particle-particle interactions. The first two terms are reminiscent of the Van Der Waals equation for simple gasses, accounting for a strong short range repulsion (A_{ij}) to simulate particle 'size' and short range attraction (London dispersion) (B_{ij}). The final term is simply the electrostatic force between charges q_i and q_j, in which the dielectric permittivity ϵ can be taken as 1 [115].

Typical simulation parameters were otherwise used. A physiologically similar bath of T = 310 K, pH = 7.0, and 0.9% NaCl aqueous solution and a time step of 2 fs. The temperature and pressure are maintained by procedures fittingly referred to as the (Berendsen) thermostat and barostat. These scale the entire system (velocities or distances, respectively) at each time step such that the desired set point temperature or pressure is approached via exponential relaxation. It is lastly important to note that the conformational state of proteins as retrieved from the data bank and the positions of molecules at the start of a simulation may be very far from what is appropriate for 'equilibrium'. Thus it is typical to allow a very short equilibration time, in this case 6 picoseconds, for these very fast relaxations to occur.

Appendix B

Algorithm to Extract α from a Stream of Sampled Data

As discussed in Section 2.4.3, the value of r is enhanced for sampling rates just above the characteristic scale of a system. For series that encompass this range, an estimate for α can be obtained by comparison with theoretical values computed via Eq. (2.50), which are unique for $1.1 \lesssim \alpha \lesssim 1.9$ (cf. Fig. 2.15). Numerically calculated maximum-r values are shown in Fig. 2.13, along with a polynomial fit. For a series X with a zero value corresponding to the position at the bottom of the parabolic potential, the estimation is done as follows:

- Create a set of undersampled series X_n's by taking every n-th value for $n = 1, 2, 3, \dots$.

- For each X_n, calculate r_n according to Eq. (4), i.e.:

  - Take the absolute value of each element.

  - For each element, subtract the subsequent element.

  - For the ensuing differences, subtract the number of negative values from the number of positive values.

  - Divide by the length of X_n minus 1.

- Find the maximum r_n, which should correspond to a peak in the trend of the ordered r_n values (as in Fig. 2.15).

- Determine the corresponding α through the curve and formula in Fig. 2.13.

Appendix C

Algorithm for the Two Reservoir System

Consider the situation in Fig. C.1 which depicts a particle in the reservoir system of Sec. 3.4. Each particle in the system has its current position $p_0 = (x_0, y_0)$ updated to a new position $\mathbf{p}_1 = (x_1, y_1)$ by the addition of a random vector with a length drawn from an alpha stable distribution. The new position must be updated to reflect the boundaries: a reflector with an opening of size d in the middle and the 'sticky' circular walls on the outside. This leads to the seven possible cases for each $\mathbf{p}_0, \mathbf{p}_1$ pair depicted in Fig. C.1. The x coordinates x_0 and x_1 may have the same or differing signs. If the signs differ, the cases differ based on what boundary the particle first encounters - the opening, the reflecting, or the sticky boundary. Then, in all but the final case, the particle may still need its trajectory truncated to remain within the reservoir.

This algorithm operates in two blocks and tries to minimize the number of steps. The first deals with the midline, updating both p_0 and p_1 to accomodate the truncation calculation in the second block.

Block 1

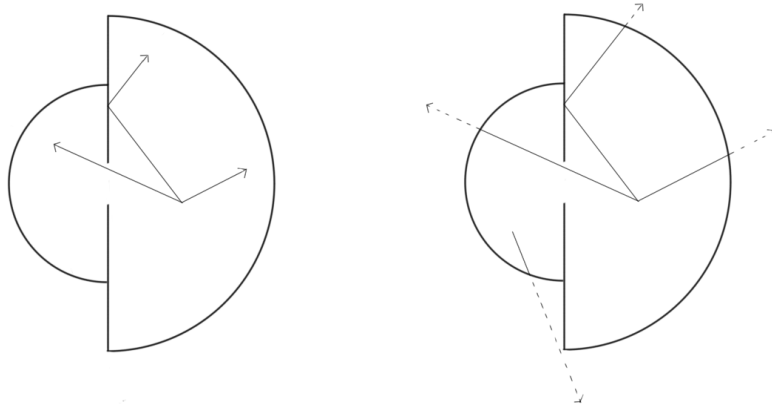- If $\text{sign}(x_0) = \text{sign}(x_1)$, exit block 1.

Figure C.1: The two reservoir system described in Sec. 3.4. There are seven possible cases of particle starting and ending positions to discriminate.

- Compute the intercept point y_I that the particle crosses $x = 0$.

- If y_I is larger than the radius of the reservoir of origin, set $\mathbf{p}_1 = (0, y_I)$ and exit block 1.

- Set $\mathbf{p}_0 = (0, y_I)$.

- If $|y_I| < d/2$, exit block 1.

- Set $\mathbf{p}_1 = (-x_1, y_1)$.

Block 2

- Compute the distance to the origin $D = \|\mathbf{p}_1\|$.

- If D is smaller than the radius of the ending reservoir, exit block 2. Which reservoir the particle finishes in can be determined by $\text{sign}(x_0 + x_1)$, where a negative result corresponds to the left reservoir.

- Truncate the remaining trajectories at the appropriate boundary. This can be accomplished by computing at when a particle starting at $\mathbf{p}_0$ with a velocity vector $\mathbf{p}_1 - \mathbf{p}_0$

94

exceeds the radius of the reservoir.

Appendix D

Traffic between the Larger and the Smaller Semicircular Reservoir

Consider the setup in Figs. 3.4 and 3.6 and let a homogeneous particle density ρ be same in both reservoirs. In this Appendix we show that, if the particles are subject to Lévy noise, accumulation in the smaller reservoir develops. Imagine a semicircular strip of width dr at a distance r from the opening. There are $\rho \pi r dr$ particles in this strip. We let the power-law approximation, cf. Eq. (2.8), be valid for $r > r_0$. Here r_0 is much larger than the width of the opening d and much smaller than the radii R_1 and R_2. The angle θ is small and with θ expressed in radians we have $d = \theta r$. For a particle in the semicircular strip at distance $r > r_0$, there is a probability that a Lévy jump will bring it to the other reservoir. To achieve such transition, the jump needs to be larger than r. For such a jump the probability is proportional to $r^{-\alpha}$. In order to go through the opening, the jump must also be in the right direction. This leads to a factor $(d/r)\cos\phi$ (cf. Fig. 3.4). After the integration from $\phi = -\pi/2$ to $\phi = \pi/2$, we derive a "direction factor" of $2d/r$, i.e. $\propto 1/r$. Putting together all of the effects specified in this paragraph, we have the following formula for the number

of transitions during a small timestep from a distance between r and $r + dr$:

$$dn^{tr}(r, r + dr) \propto \frac{1}{r} r^{-\alpha} r \, dr = r^{-\alpha} \, dr. \tag{D.1}$$

Next we integrate from r_0 to the boundary R_i ($i = 1, 2$) and find for the number of Lévy-jump-associated transitions from reservoir i:

$$N_i^{tr} \propto \int_{r_0}^{R_i} r^{-\alpha} \, dr \propto \text{sgn}(1 - \alpha) \left(R_i^{1-\alpha} - r_0^{1-\alpha} \right). \tag{D.2}$$

Care must be taken in case of $\alpha = 1$. In that case $N_i^{tr;\alpha=1} \propto \log R_i - \log r_0$. We thus conclude that for $0 < \alpha \leq 1$, the number N_i^{tr} diverges as R_i is taken to infinity. For $1 < \alpha < 2$ a constant value for N_i^{tr} ensues if $R_i \to \infty$.

The proportionality constant (associated with the $\propto$) and the r_0 (the radius from which the power law is taken to describe the Lévy distribution) are the same for both reservoirs. So if both reservoirs in Figs. 3.4 and 3.6 have the same uniform ρ, then we find for the net number of particles $\Delta N^{tr} = N_1^{tr} - N_2^{tr}$ that transits from the larger to the smaller reservoir:

$$\Delta N^{tr} \propto \text{sgn}(1 - \alpha) \left(R_1^{1-\alpha} - R_2^{1-\alpha} \right). \tag{D.3}$$

If $0 < \alpha \leq 1$ and if values for R_1 and R_2 are large, then there is accumulation in the smaller reservoir.

For $1 < \alpha < 2$ there will again be accumulation in the smaller reservoir, but the effect gets smaller as R_2 and R_1 grow and will become negligible as $R_{1,2} \to \infty$. Effectively, the geometry of the reservoirs is irrelevant for large R_1 and R_2. In that case it is particles near the opening that dominate the traffic through the opening.

In the main text the above derivation is carried out for the case of a density $\rho_i(r_i)$ ($i = 1, 2$) that depends on the distance r_i from the opening.

Finally, it is worth pointing out that the above derivation readily generalizes to higher

dimensional reservoirs. In the 3D case we face hemispheres. The number of particles in a hemispheric shell is $\rho 2\pi r^2 dr$. For the nD case, the shell contains a number of particles that is proportional to $r^{n-1}dr$. We thus have for dn_{nD}^{tr}:

$$dn_{nD}^{tr}(r, r + dr) \propto \frac{1}{r} r^{-\alpha} r^{n-1} \, dr = r^{n-2-\alpha} \, dr. \tag{D.4}$$

This leads to:

$$N_{i,nD}^{tr} \propto \int_{r_0}^{R_i} r^{n-2-\alpha} \, dr \propto \left(R_i^{n-1-\alpha} - r_0^{n-1-\alpha} \right). \tag{D.5}$$

and

$$\Delta N_{nD}^{tr} \propto \left(R_1^{n-1-\alpha} - R_2^{n-1-\alpha} \right). \tag{D.6}$$

This is an interesting result. For 3 and more dimensions, we do not need to discriminate between different ranges of α. Lévy noise with any α ($0 < \alpha < 2$) will in that case lead to a significantly higher density in the smaller reservoir and the effect will be stronger for higher values of $R_{1,2}$.

Appendix E

Rights and Permissions

All images in this work were created for this work, have copyrights owned by the author of this work, or have the expressed permission for their use from those holding the copyright. The following document shows legal permission for those images with copyrights held by other parties.

American Physical Society
Reuse and Permissions License

01-Apr-2022

This license agreement between the American Physical Society ("APS") and Steven Yuvan ("You") consists of your license details and the terms and conditions provided by the American Physical Society and SciPris.

Licensed Content Information

License Number:	**RNP/22/APR/052115**
License date:	01-Apr-2022
DOI:	10.1103/PhysRevE.104.014119
Title:	Breaking of time-reversal symmetry for a particle in a parabolic potential that is subjected to Levy noise: Theory and an application to solar flare data
Author:	Steven Yuvan and Martin Bier
Publication:	Physical Review E
Publisher:	American Physical Society
Cost:	USD $ 0.00

Request Details

Does your reuse require significant modifications: No

Specify intended distribution locations:	United States
Reuse Category:	Reuse in a thesis/dissertation
Requestor Type:	Author of requested content
Items for Reuse:	Whole Article
Format for Reuse:	Electronic

Information about New Publication:

University/Publisher:	East Carolina University
Title of dissertation/thesis:	Lévy noise induced steady states
Author(s):	Steven Yuvan
Expected completion date:	May. 2022

License Requestor Information

Name:	Steven Yuvan
Affiliation:	Individual
Email Id:	yuvans16@students.ecu.edu
Country:	United States

American Physical Society
Reuse and Permissions License

TERMS AND CONDITIONS

The American Physical Society (APS) is pleased to grant the Requestor of this license a non-exclusive, non-transferable permission, limited to Electronic format, provided all criteria outlined below are followed.

1. You must also obtain permission from at least one of the lead authors for each separate work, if you haven't done so already. The author's name and affiliation can be found on the first page of the published Article.

2. For electronic format permissions, Requestor agrees to provide a hyperlink from the reprinted APS material using the source material's DOI on the web page where the work appears. The hyperlink should use the standard DOI resolution URL, http://dx.doi.org/{DOI}. The hyperlink may be embedded in the copyright credit line.

3. For print format permissions, Requestor agrees to print the required copyright credit line on the first page where the material appears: "Reprinted (abstract/excerpt/figure) with permission from [(FULL REFERENCE CITATION) as follows: Author's Names, APS Journal Title, Volume Number, Page Number and Year of Publication.] Copyright (YEAR) by the American Physical Society."

4. Permission granted in this license is for a one-time use and does not include permission for any future editions, updates, databases, formats or other matters. Permission must be sought for any additional use.

5. Use of the material does not and must not imply any endorsement by APS.

6. APS does not imply, purport or intend to grant permission to reuse materials to which it does not hold copyright. It is the requestor's sole responsibility to ensure the licensed material is original to APS and does not contain the copyright of another entity, and that the copyright notice of the figure, photograph, cover or table does not indicate it was reprinted by APS with permission from another source.

7. The permission granted herein is personal to the Requestor for the use specified and is not transferable or assignable without express written permission of APS. This license may not be amended except in writing by APS.

8. You may not alter, edit or modify the material in any manner.

9. You may translate the materials only when translation rights have been granted.

10. APS is not responsible for any errors or omissions due to translation.

11. You may not use the material for promotional, sales, advertising or marketing purposes.

12. The foregoing license shall not take effect unless and until APS or its agent, Aptara, receives payment in full in accordance with Aptara Billing and Payment Terms and Conditions, which are incorporated herein by reference.

13. Should the terms of this license be violated at any time, APS or Aptara may revoke the license with no refund to you and seek relief to the fullest extent of the laws of the USA. Official written notice will be made using the contact information provided with the permission request. Failure to receive such notice will not nullify revocation of the permission.

14. APS reserves all rights not specifically granted herein.

15. This document, including the Aptara Billing and Payment Terms and Conditions, shall be the entire agreement between the parties relating to the subject matter hereof.